Spreading ceramic stereolithography pastes: Insights from shear- and orthogonal-rheology

Sylvain Fournier, Jérôme Chevalier, Saray Perez-Robles, Claudia Carotenuto, Mario Minale, Helen Reveron, Guilhem P. Baeza

Spreading Ceramic Stereolithography Pastes: Insights from Shear- and Orthogonal-Rheology

Sylvain Fournier,[1] Jérôme Chevalier,[1] Saray Perez-Robles,[2] Claudia Carotenuto,[2] Mario Minale,[2] Helen Reveron,[1] and Guilhem P. Baeza[1]

[1)]*Univ Lyon, INSA Lyon, Université Claude Bernard Lyon 1, CNRS, MATEIS, UMR5510, Villeurbanne, 69621, France*

[2)]*University of Campania "Luigi Vanvitelli", Department of Engineering, Real Casa dell'Annunziata via Roma 29, 81031 Aversa (CE), Italy*

(*Electronic mail: guilhem.baeza@insa-lyon.fr ; sylvain.fournier@insa-lyon.fr)

(Dated: 25 October 2023)

We study the shear rheological behavior of a commercial stereolithography paste containing ≈ 50 vol.% of zirconia particles (diameter ≈ 100 nm) with the aim to clarify physical mechanisms occurring during the "scraping" step of this yield stress fluid. Beyond a flow curve characterized by a high zero-shear viscosity accompanied with an overall shear-thinning behavior, we investigate in a systematic way the transient regime through start-up experiments. We demonstrate that a structural transition occurs between $10^{-2}\,s^{-1}$ and $10^{-1}\,s^{-1}$ resulting in an apparent interruption of the shear-thinning. The corresponding transient response presents a pronounced extra-growth of the shear stress before to stabilize at high strain amplitude and a negative first normal stress difference peak, both effects becoming stronger at higher shear rates. These observations are rationalized based on the high interparticle friction owing to the polyhedral shape and the roughness of the particles. Besides, relaxation tests following the start-up experiments reveal that the samples submitted to shear rates higher than $10^{-1}\,s^{-1}$ cannot relax the shear stress to the same level as in low shear rate experiments, suggesting a durable structural modification likely to impact the quality of the parts prior to their debinding and densification. Finally, we utilize orthogonal superposition rheology to illustrate how the application of an oscillatory deformation during the scraping procedure could help to reduce the shear-thinning interruption and improve the stereolithography processing as already observed empirically during scraping.

I. INTRODUCTION

The emergence of additive manufacturing technologies requiring well-controlled mechanical properties of the processed material both in the liquid and solid states has considerably widened the interest of engineers for rheology, regardless of the type of material (e.g., polymers[1], metals[2] and ceramics[3]). In the latter case, several strategies relying on the design of a viscoelastic material containing a high volume fraction of nano- or micro-particles ($\Phi >$ 40 vol.%) have been successfully implemented such as direct ink writing (or robocasting)[4], fused filament fabrication[5], vat-photopolymerization methods (including liquid laser-based, digital light processing and mask-projection[6–8]), and paste stereolithography (denoted SLA hereafter)[9].

The SLA technique consists of spreading a thin layer of paste and photopolymerize a pattern before repeating the procedure to achieve the manufacturing of "green" (i.e., raw printed) parts, possibly characterized by a high geometrical complexity[8]. The residual non-polymerized paste is then washed out and the green part is subsequently "debinded" (organic species are eliminated from $T = 50\,°C$ up to $400\,°C$) and finally sintered (between $800\,°C$ and $1700\,°C$) to obtain a strong densified ceramic object. This commercially available technology is growingly used in various industrial fields including but not limited to bio-engineering for the design of personalized bone implants[10]. Typical SLA pastes are essentially made of ca. $\Phi \approx 50$ vol.% of ceramic particles (e.g., alumina, zirconia) and two or more photopolymerizable monomers that form a thermoset resin once irradiated by a UV laser of a typical wavelength of 355 nm or 405 nm. Other components like photoinitators, dispersants and additional polymers are also included to optimize the processing route. The composition of commercial pastes is however kept confidential and the numerous variables investigated in the academic literature[11,12] makes it quite difficult to extract a canonical recipe where the role of each ingredient on rheological and curing properties is clearly identified. Promising work mainly based on rheological flow curves consisting of following the steady-shear viscosity in the permanent regime as a function of the shear rate ($\eta = f(\dot{\gamma})$) have nevertheless been published on the impact of dispersants and plasticizers[11–14].

One of the main challenges regarding the SLA technology resides in the appropriate spreading of the paste, which is conducted through a scraper blade that typically operates at a few mm s^{-1} to form 25 µm to 100 µm thick layers, corresponding therefore to an effective processing shear rate of $\dot{\gamma}_{SLA} \approx 10^2\,s^{-1}$. This step is actually of great importance since a rough deposition immediately leads to defects in the green parts causing stress concentration that will ultimately result in the failure of the material during subsequent debinding and sintering steps or insufficient strength of the resulting parts[15]. Appropriate rheological properties mainly require i) a relatively high zero shear viscosity, or as in the present case, a yield stress fluid behavior that promotes the material's self-standing, and ii) a pronounced shear-thinning behavior ensuring a homogeneous spreading at the processing shear rate. While the former is of extreme importance for the robocasting technology where the paste is deposited with a syringe, it is less critical in SLA since the laser rapidly crosslinks most of the organic phase. More importantly, shear-thinning is a key process that will ensure the quality of the green parts pro-

duced through SLA. Noteworthy is the fact that the establishment of a precise definition of the printability for different additive manufacturing technologies (and materials) is currently an active field of research[1,3,16]. The ternary nature of SLA pastes, i.e., that contain 1) small molecules acting as a solvent (prior to polymerization), 2) polymers playing the role of dispersant and/or plasticizers and 3) polydisperse inorganic particles, makes it tempting to compare them to other non-model systems. In fact, one can think of other ternary mixtures like oil tailings[17,18] or bitumen-based composites[19] that also contain the three above-mentionned phases. Oil tailings notably contain 30 wt% of nanoparticles and ca. 2 wt% of bitumen, the rest being water. On the other hand, although bitumen-based composites used for road application contain a higher fraction of hard fillers, they mainly consist of micro- and millimetric particles. It therefore appears that SLA pastes (containing ca. 50 vol% of inorganic nanofillers) embedded into an inorganic mixture possess a quite unique formulation providing them with a unique place in the vast rheological landscape. Because SLA pastes contain a high fraction of submicronic particles dispersed in a molecular liquid, we believe that they can be comprehended as colloidal gels where the rheological properties strongly depend on the solid loading, particles size and shape, and interparticle interactions[20]. Regarding the latter point, SLA pastes usually contain a significant fraction of dispersant consisting of amphiphilic molecules that adsorb at the particles surface in order to prevent permanent aggregation upon shearing and limit the material ageing at rest[21]. Yet, the stability of SLA pastes hardly exceeds a few months.

At very low deformation (linear regime), colloidal gels exhibit constant storage (G') and loss (G'') dynamic moduli corresponding to equivalent structures at various strain amplitudes. This first regime is mostly rationalized by invoking "colloidal cages" in which a given particle conserves the same neighbors and the average number of contacts is not affected by the external force. The stress threshold separating this regime from shear-thinning tends to decrease upon increasing the solid loading because of further chaotic interactions caused by additional and stronger interparticle contacts. Above this limit, particles gain enough mobility to escape from their cage resulting in energy dissipation and yielding[22–24]. In the shear-thinning regime, the viscosity is seen to continuously decrease owing to the particles local rearrangement along with the flow direction ("local layering"), reducing the average number of frictional contacts[25]. This state is reachable from very limited particles motion as demonstrated by oscillatory shear experiments where viscosity loss was observed from the very first strain cycle[26]. In the presence of pre-aggregated objects, shear-thinning can alternatively be seen as the size reduction of superstructures causing a "hydrodynamical" (rather than "frictional") decrease of the viscosity[27] - this vision however concerns materials with low solid loadings, making it irrelevant in the present work.

While the above-mentioned scenario is usually observed experimentally at low and intermediate shear rates, a non-monotonic evolution of the viscosity, corresponding to shear-thickening mechanisms, is often observed when the shear rate is further increased. Generally speaking, one can define the shear-thickening onset as the transition from lubricated to frictional flow[28–30] in non-Brownian suspensions, essentially corresponding to the formation of transient (hydro)clusters[30–33] capable of holding a large amount of stress by breaking and reforming under the bulk shearing motion[34,35]. Importantly, clustering is promoted by particles roughness and shape anisotropy that involve sliding and rolling friction as well as interlocking hindrance, which limit particles motion[34,36]. On the other hand, stabilizing particles through steric repulsion based on polymer brushes tends to favor lubricated contacts, helping to unlock particles that can better adapt to the flow[37].

Because shear-thickening instabilities often result in a macroscopic texturing of the materials, they have a direct impact on the spreading quality of SLA pastes (usually made of both rough and polyhedral particles). The goal of the present article is therefore double. (1) We first investigate in-depth the rheological behavior of a commercial SLA paste by performing steady-shear experiments to qualitatively mimick the spreading of the paste. While most of the rheological studies on this type of materials is restricted to the measurement of flow curves and dynamic strain sweeps[11,12,14], we investigate in a systematic way the transient regime through start-up experiments, following both shear and normal stresses, which enable us to provide a structural description of the material upon increasing the shear rate. (2) Second, we demonstrate how shear-thickening events, being deleterious for the SLA process, can be limited or suppressed by using orthogonal superposition rheology. This quantitative analysis supports previously reported empirical observations (e.g. Pateloup et al.[38]) that invite therefore the ceramic additive manufacturing community to adopt such characterization techniques.

II. MATERIALS AND METHODS

A. Materials

In this work, we study a commercially available ceramic stereolithography paste 3Y-F01 (3DCERAM Sinto, France). It exhibits a solid-like behavior at rest and is designed to be used in 3DCERAM Sinto stereolithography printers. It is composed of yttria-stabilized zirconia (ZrO_2 with 3 mol.% of Y_2O_3) polydisperse particles of ca. 90 nm in diameter. The corresponding solid loading is ca. 49 vol.% (determined from thermogravimetric analysis assuming a density of 6.1 g cm^{-3} for the zirconia and 1.3 g cm^{-3} for the organic phase). The rest of the paste mainly consists of acrylate monomers and oligomers and a small amount of photoinitiators. In addition, a dispersant is added to stabilize the particles, allowing to enhance the solid loading while limiting the ageing of the paste (typically acids or esters are used as electro-steric repulsors[9]). Other components such as PEG of hundreds of g mol^{-1}, acting as a "plastifying binder", can also be added to enhance constraint release during the debinding step while slightly modifying the paste viscosity[9,11].

B. Methods

1. Structural analysis: SEM, SAXS-USAXS

The "wet" ceramic paste and "dry" ceramic particles obtained from a thermally debinded (organic-free) paste sample were characterized by Scanning Electron Microscopy (SEM, Zeiss SUPRA VP55, Switzerland) at 10 kV, 5.92 mm working distance and 3 10^4 magnification. A lower voltage (1 kV) and a shorter working distance (2.9 mm) were used to observe the (non-conducting) particles at ca. 2.5 10^4 magnification enabling to enhance size distribution measurements.

Particle size measurements and image analysis were performed with ImageJ (National Institutes of Health, USA). The Particle Size Distribution (PSD) was obtained by measuring the area of 500 particles from several zones in a SEM image. Because of the non-spherical nature of the particles, the "projected area diameter" or "equivalent spherical diameter" d_A was used as a relevant parameter to describe the PSD. d_A is defined as the diameter of a disk that has the same area as the actual particle.

SAXS-USAXS measurements were performed on beamline ID02 at the European Synchrotron Radiation Facility (ESRF, Grenoble, France). Thin layers of paste (70 µm) were sandwiched with Kapton tape and measured at three sample-detector distances (1 m, 10 m and 31 m) resulting in a momentum transfer range spanning $3\ 10^{-3}\ \mathrm{nm}^{-1} < ||\vec{q}|| < 3.5\ \mathrm{nm}^{-1}$. Ten acquisitions of 200 ms exposure time separated by 0.1 s were averaged for each scattering measurement. Beam energy was set to 17 keV to overcome the strong X-rays absorption of zirconia. Note that higher beam energy coincided with zirconia absorption bands.

2. Shear rheology

A strain-controlled ARES-G1 (2kFRTN1 transducer) rheometer (Rheometric Scientific, currently TA, USA) equipped with a stainless steel cone-plate geometry of diameter 25 mm (CP25) (angle: 0.1 rd, gap: 51 µm) was used to perform start-up experiments varying the shear-rate from $\dot{\gamma} = 3.2\ 10^{-4}\ \mathrm{s}^{-1}$ to $3.2\ \mathrm{s}^{-1}$. In addition, a cone-plate geometry consisting of a 8 mm diameter plate and a 25 mm diameter cone (CP8) (angle: 0.1 rd, gap: 51 µm) was used to perform additional start-up experiments varying the shear rate from $\dot{\gamma} = 10^{-1}\ \mathrm{s}^{-1}$ to $31.6\ \mathrm{s}^{-1}$. Changing the diameter of the plate geometry enabled to discard possible wall-slip effects, which is further confirmed by a gap variation reported in Supplementary Material (SM) Section S-I. A cone-partitioned plate geometry must have helped to delay edge fracture instabilities.[39] All the experiments were conducted at 20 °C ± 1 °C where the paste is very sticky and behaves as a yield stress fluid.
The overall start-up test routine was conducted as follows. After the loading of a fresh sample, a preconditioning shear step was applied through a dynamic strain sweep test from $\gamma = 3.2$ to $\gamma = 10^{-4}$ at $10\ \mathrm{rd\ s}^{-1}$. After ca. 200 s, ensuring the paste relaxation (see SM section S-II), a dynamic frequency sweep was performed at $\gamma = 3.2\ 10^{-4}$ from $\omega = 10^2\ \mathrm{rd\ s}^{-1}$ to $10^{-1}\ \mathrm{rd\ s}^{-1}$ to control the sample state before non-linear testing. Note that such deformation amplitude was the lowest achievable by the rheometer enabling to limit as much as possible non-linear effects during the dynamic frequency sweep tests. The next step was the start-up experiment by itself, consisting of the application of a constant shear rate to the paste (from $\dot{\gamma} = 3.2\ 10^{-4}\ \mathrm{s}^{-1}$ to $31.6\ \mathrm{s}^{-1}$). The maximal deformation was systematically set to $\gamma_{max} = 63$, corresponding to a whole revolution of the geometry being sufficient to reach the steady state. Both the transient shear stress (σ^+) and the first normal stress difference (N_1) were recorded and analyzed. The stress relaxation σ^- was then measured for 120 s.

Axial compliance characteristic time for the 2kFRTN1 transducer t_a is estimated to be $t_a(\dot{\gamma}) = 1.2\ 10^{-4}\ \eta_{SS}(\dot{\gamma})$ according to Venerus et al.[40] The material's characteristic time can be evaluated with $\tau_{mat}(\dot{\gamma}) = \eta_{SS}(\dot{\gamma})/G_0 = 4.4\ 10^{-5}\ \eta_{SS}(\dot{\gamma})$ with $G_0 = G'(\gamma \to 0)$ resulting in $t_a/\tau_{mat} = 2.71$. Because this ratio is slightly higher than 1, axial compliance effects cannot be fully excluded. On the other hand, N_1 was not seen to relax in the measuring time window (Fig. 7a), indicating that its characteristic relaxation time τ_N is larger than 120 s, in agreement with the fact that a full relaxation of σ^- was never observed. Since $\tau_N >> t_a$, normal force measurement delay is not expected.[41]

Importantly, in the present case, (3Y-F01 paste from 3DCERAM), the typical layers thickness is set to $e = 25$ µm to obtain highly resolved and well polymerized 3D-printed parts and the speed of the scraper is close to $v_{scrap} = 2.5\ \mathrm{mm\ s}^{-1}$, both parameters playing an important role on the duration of the SLA process, being a major challenge in the industry. The resulting shear rate experienced by the paste during the procedure reaches therefore values of ca. $\dot{\gamma}_{SLA} = v_{scrap}/e = 10^2\ \mathrm{s}^{-1}$.

3. Orthogonal superposition rheology

Orthogonal SuperPosition (OSP) rheology experiments were performed with a strain-controlled ARES-G2 rheometer (TA Instruments, USA) equipped with an open bottom double-wall concentric Couette geometry. The exact dimensions of the 1 mm gap geometry were $R_1 = 13.8675$ mm ; $R_2 = 14.6965$ mm; $R_3 = 16.0385$ mm ; $R_4 = 16.998$ mm ; $l = 51.652$ mm and $h = 43.652$ mm. We refer the reader to SM Section S-III where we provide a graphical representation of the geometry adapted from Tao et al. article[42]. Loading the material in the geometry was particularly challenging considering its very high viscosity. The paste had to be extruded with a syringe in the lower part of the geometry in order to fill it. Following paste loading, a small rotation of the lower part was needed to allow the downward displacement of the upper part. Once the upper part of the geometry reached the measuring distance from the bottom (8 mm), the sample covered the whole side surface of the top geometry ensuring a correct measurement. Before each experiment, the sample was pre-sheared following a flow curve profile from $\dot{\gamma} = 3.2\ \mathrm{s}^{-1}$ to $10^{-4}\ \mathrm{s}^{-1}$. Two types of measurements were then performed:
i) Rotational dynamic frequency sweep experiments were first conducted in the tangential plane (||) serving as a reference.

They were then repeated in the vertical direction ($\perp$) without rotational shear. The amplitude of the normal strain was chosen as small as possible to limit non-linear effects while considering the limitations of the transducer at low displacements. A compromise deformation of $\varepsilon = 3\ 10^{-3}$ corresponding to $dL = 2.76\ 10^{-3}$ mm was identified as the best option. The recorded data was limited to the frequency window ω 0.5 rd s^{-1} – 50 rd s^{-1} due to normal strain (ε) deviations. Orthogonal dynamic frequency sweep tests were then performed under $\parallel$ steady shear for shear rates value of: $\dot{\gamma} = 10^{-3}$ s^{-1} ; 10^{-2} s^{-1} ; 10^{-1} s^{-1} ; 1 s^{-1} and 10^{1} s^{-1}.
ii) Flow curves with "normal vibrations" were performed from $\dot{\gamma} = 10$ s^{-1} to $1.8\ 10^{-3}$ s^{-1}. The superimposed oscillatory normal strain was set for each measurement to the maximal available amplitude $\varepsilon = 5\ 10^{-2}$ and $\omega_{\perp} = 1$ rd s^{-1} ; 3.2 rd s^{-1} ; 10 rd s^{-1} and 100 rd s^{-1}. An additional test was performed with a lower normal strain amplitude: $\varepsilon = 5\ 10^{-3}$ at $\omega_{\perp} = 100$ rd s^{-1}.

End-effect factors were applied on both data recorded in $\parallel$ and $\perp$ directions when using the OSP device. The first correction consisted of considering the "primary end-effect factor" c_L relating the viscosity measured with classical cone-plate geometry and the one measured in rotation ($\parallel$) with the OSP device such as: $\eta_{OSP\parallel} = \eta_{OSP\parallel(recorded)}/c_L$. This factor arises from the non-uniform shear rate distribution over the annular cross-section of the geometry. The second correction consisted of considering the "orthogonal end-effect factor" c_{Lo} relating the viscosity measured with a classical cone-plate geometry with the one measured in the vertical direction ($\perp$) with the OSP device such as: $\eta^*_{OSP\perp} = \eta^*_{OSP\perp(recorded)}\ c_{Lo}$. This factor mainly concerns the correction of the pumping effect generated by the bob motion, which is expected to differ between a solid-like paste at rest and a low-viscosity Newtonian fluid.

Investigating Newtonian fluids of various viscosities, Tao et al.[42] nevertheless pointed out that the correction factors were different from the manufacturer's ones, emphasizing therefore possible ambiguities.[43] To the best of our knowledge, no similar study is available for non-Newtonian fluids making the evaluation of the end-effect factors quite intricate when dealing with nonlinear deformation. In the present study, both factors are thus expected to depend strongly on the strain (and shear rate) amplitude. For example, flow curves measured with the ARES-G2 OSP geometry and the ARES-G1 CP25 geometry resulted in a good overlap of the data for a correction coefficient of $c_L^{FC} = 0.14$. However, because dynamic frequency sweeps performed with the OSP device in the vertical direction ($\perp$) could not be run in the linear regime (see SM Section S-III), we decided not to apply an arbitrary $c_{Lo}^{DFS\perp}$ coefficient to the data.

III. RESULTS AND DISCUSSION

A. Structural analysis

We present in Fig.1a the SAXS intensity over three decades of scattering vector ($q = ||\vec{q}||$) enabling to extract the main structural characteristics of the paste.

At $q > 10^{-1}$ nm^{-1}, in the so-called Porod regime, the intensity varies as $I \sim q^{-3.8}$ indicating a rather sharp interface between dense particles and the organic background (no porosity) with, however, a significant surface roughness. In fact, the intensity at "large" q (i.e., $q > 2\pi/d_A$) scales as $I \sim q^{(6-D_s)}$, where D_s is the fractal dimension of the interface, which, if higher than 2, emphasizes the presence of surface asperities[44]. Also, the absence of oscillations of the form factor in this q-range is a clear indication of the high polydispersity of the particles. At $q \approx 3.5\ 10^{-2}$ nm^{-1}, the intensity exhibits a major break-in slope corresponding to the Guinier regime of the particles together with the presence of a strong inter-particles structure factor[45] owing to the high volume fraction in scattering objects ($\Phi = 49$ vol %). Importantly, while no major constructive interferences (upward peak) is observed at $q = q^*$ because of the large polydispersity of the particles[45], a "correlation hole", pushing down the intensity at $q < q^*$ is detectable through the change in slope observed close to $q = 10^{-2}$ nm^{-1}. Although an accurate estimation of the average radius of the particle is difficult here, the Kratky representation displayed in the inset suggests a diameter of ca. $d_p = 2\pi/q^* \approx 195$ nm.

At lower q, the scattering intensity seems to converge towards a plateau starting from q^{**} ca. 40 times higher than the intensity detected at q^*. This estimation can be made by using the ratio of the prefactors I_{0-i} of the Guinier model[44] applied both around q^* and q^{**} such as $I(q) = I_{0-i}\ exp(\frac{-q^2R_i^2}{3})$ where $R_i \approx \pi/q^*$ or π/q^{**} (see Fig.1). Importantly, the absence of divergence at low-q excludes the presence of macrophase-separated agglomerates in the paste. This observation is further supported by the fact that $q^{**}/q^* \approx 7$ (see inset Fig.1a) that one can use to connect the number of particles in the agglomerates (N_{agglo}) and their characteristic diameter ($d_{agglo} \approx 2\pi/q^{**}$). In fact, by assuming a relatively open inner structure of the agglomerates corresponding to a volume fractal dimension $D_f = 2$, one can satisfyingly write $N_{agglo} = I(q^{**})/I(q^*) \approx 40$ and $N_{agglo} = (d_{agglo}/d_p)^{D_f} \approx 49$.

This "representative" or "statistical" SAXS characterization is completed by a local analysis through SEM for both the "wet" paste and the "dry" debinded particles in Fig.1b. While the paste clearly reveals the presence of discrete objects, likely to correspond to a few particles surrounded by a layer of organic matter, observing the "dry" particles confirms their high polydispersity, both in terms of size and shape. The corresponding image analysis presented in Fig.1c indicates a log-normal particle size distribution with the most probable diameter being close to 81 nm and an average of $\overline{d_p^{SEM}} \approx 96$ nm.

The discrepancy between $\overline{d_p^{SEM}}$ and d_p is explained by the fact that while SEM estimations are based on the discrimination of the borders of all the particles (including the merged ones), SAXS ones rather rely on the fluctuation of density in the paste. In the latter case, individual particles belonging to small and dense aggregates are therefore not resolved, which results in a higher estimation of the "particles" size. We illustrate this effect in Fig.1b where we have highlighted in red the borders of a few single particles forming a dense aggregate having a diameter ca. twice as large than its elementary

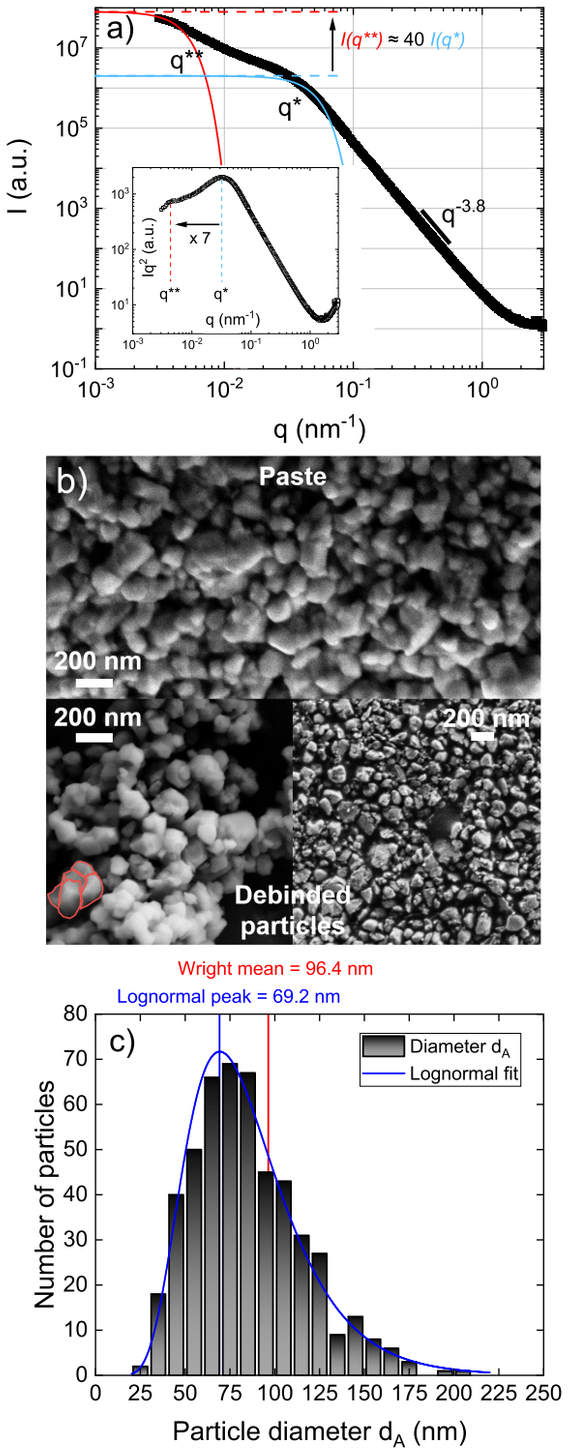

FIG. 1. a) SAXS intensity measured on the 3Y-F01 paste. Solid lines are Guinier fit[44] enabling to approximate N_{agglo} (see text). Inset: Kratky representation of the analogous data. b) SEM observation of the paste (top) and the debinded powder (bottom left and bottom right). The borders of a dense aggregate and its building blocks are highlighted in red (see text). c) Particle size distribution obtained from the debinded powder micrograph.

building blocks.

B. Steady shear experiments

In this section, we investigate the rheological behavior of the SLA paste by using two different procedures: i) "flow curves", consisting of measuring the viscosity of the paste at equilibrium (steady-state) for increasing (or decreasing) values of the shear rate, and ii) "start-up" experiments, consisting of measuring the viscosity as a function of time (or strain) at a given shear rate, from the transient regime up to the steady state. These experiments are highly relevant for both the fundamental understanding of the rheological properties and for the processing.

The most common rheological characterization performed by researchers in ceramics additive manufacturing is the flow curve[12,14]. In fact, it allows to measure the global shear-thinning behavior of the paste rapidly, providing a relevant value of the steady-state viscosity at a targeted shear rate. We present in Fig.2 the corresponding measurement for the 3Y-F01 paste, performed both by increasing the shear rate (solid line) and decreasing it (dashed line). As expected, these preliminary tests reveal a strong shear-thinning behavior together with a quite high viscosity at low shear rate, both characteristics being respectively required for the scraping ability and the self-standing behavior of the paste. The similitude of the two flow curves indicates that multiple steady shear steps do not cause significant permanent modifications of the particles structure. Yet, the non-overlap of the curves highlights the thixotropic behavior of the material. It is interesting to notice that the shear-thinning trend is interrupted between $\dot{\gamma} = 10^{-2}\,\mathrm{s}^{-1}$ and $\dot{\gamma} = 10^{-1}\,\mathrm{s}^{-1}$, without however leading to a growth of the viscosity that would have corresponded to a formal shear-thickening event. At higher shear rate ($\dot{\gamma} > 10^{-1}\,\mathrm{s}^{-1}$), the exponent of $\eta(\dot{\gamma})$ is -0.86, which indicates that the stress keeps on growing and that shear-banding does not dominate the response of the material.

This interruption invites us therefore to deepen the rheological characterization of our SLA paste. Since its origin is very likely to be hidden in the transient regime, we have performed start-up experiments and reported the corresponding steady-state viscosities in Fig.2. We used two different CP diameters: 8 mm (black disks) and 25 mm (black crosses), with the aim of extending the range of shear rates. Despite the presence of an apparent shear-thickening event at $\dot{\gamma} = 3.2\ 10^{-2}\,\mathrm{s}^{-1}$, the so-obtained data match remarkably well the flow curves (including in the gold panel of Fig.2), which validates our methodology and provides reliable data in the transient regime, as presented in Fig.3. The viscoelastic response (dynamic frequency sweep) at the lowest strain available is reported in SM Section S-IV, confirming that the paste is systematically in the same state prior to the start-up experiments.

In Fig.3, we present the transient viscosity as a function of time $\eta^+(t)$ for various shear rates. As anticipated, these data make emerge an envelope, which however does not strictly represent the linear behavior of the paste as the data at the lowest shear rate ($\dot{\gamma} = 3.2\ 10^{-4}\,\mathrm{s}^{-1}$) already presents signs

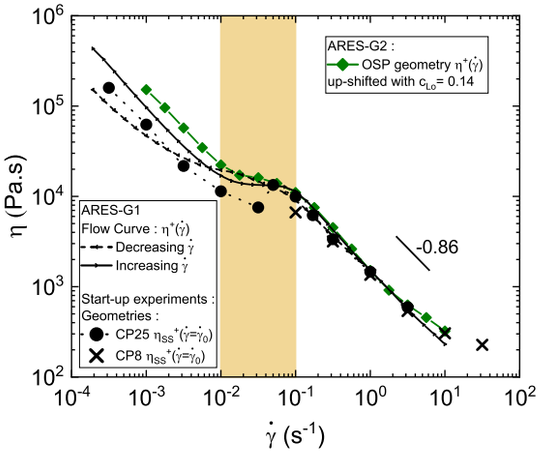

FIG. 2. Flow curves obtained with different rheometers/geometries compared with flow curve reconstructed from the plateau of start-up tests. Area highlighted in gold in shear-thinning slowdown zone for $\dot{\gamma}$ between $10^{-2}\,s^{-1}$ & $10^{-1}\,s^{-1}$.

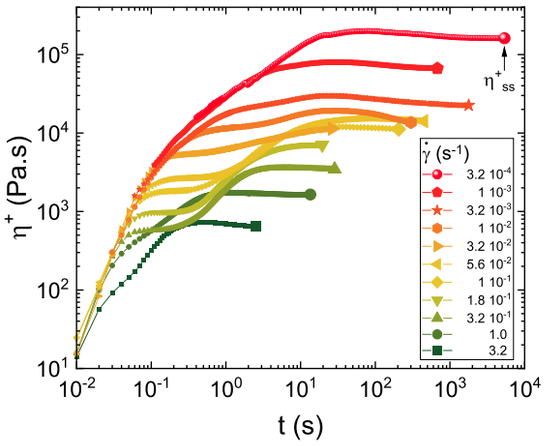

FIG. 3. Viscosity – time representation of start-up tests performed at different shear rates

of non-linearity. In fact, while one could have expected a linear growth of the viscosity followed by a plateau at long time, the envelope conversely exhibits two successive breaks in slope ($t = 10^{-1}$ s and $t = 10^{1}$ s) and a slight overshoot of the viscosity before completely stabilizing. This behavior, most likely caused by the high solid loading, suggests therefore that the true linear regime is restricted to deformation smaller than $\gamma \approx 3\ 10^{-5}$, hardly accessible in oscillatory rheology with a conventional rheometer. In spite of their good reproducibility, it also indicates that the above-mentioned dynamic frequency sweep tests were performed slightly in the non-linear regime. More interestingly, while the steady-state viscosity η_{SS} is seen to decrease with increasing the shear rate, approaching $\dot{\gamma} = 10^{-2}\,s^{-1}$ (that corresponds to the low-limit of the plateau in Fig.2) induces a significant growth of the viscosity with time (denoted "build-up" hereafter), well beyond the first yield-point at which data diverge from the envelope. Whereas the viscosity eventually decreases at long time for $\dot{\gamma} = 3.2\ 10^{-2}\,s^{-1}$ and $\dot{\gamma} = 10^{-2}\,s^{-1}$, it remains at a high level for higher shear rates, which unambiguously confirms the transition observed in flow curves and the corresponding plateau at $\eta \approx 10^4$ Pa s.

To clarify the physical origin of such complex rheological behavior, we present in Fig.4 the corresponding shear stress σ^+ (a) and the first normal stress difference $N_1 = \sigma_{11} - \sigma_{22}$ (b) as a function of the shear strain.

Note that η^+, σ^+ and N_1 data in Fig. 3,4a-b are cut as soon as edge fracture instabilities are suspected, corresponding to a sudden and large decrease of N_1, as demonstrated by Andrade et al.[46] through series of photographs. Actually, edge fracture instabilities at $\dot{\gamma} = 10^{-2}\,s^{-1}$ and $3.2\ 10^{-2}\,s^{-1}$ do not allow to reach a true viscosity and shear stress plateau respectively in Fig.3 and 4a.

These representations (Fig.4a-b) evidence once more the rheological transition through the evolution of various parameters. First, while the yield strain and the yield stress are seen to be independent of the shear rate for $\dot{\gamma} \leq 3.2\ 10^{-3}\,s^{-1}$, corresponding respectively to $\gamma \approx 10^{-2}$ and $\sigma^+ = 70$ Pa (Fig.4a), the yield stress increases significantly at higher shear rates, reaching ca. 200 Pa at $\dot{\gamma} = 3.2\,s^{-1}$. Second and more strikingly, a quick look at high strain amplitude emphasizes the presence of a group of low shear rate experiments where the steady-state shear stress σ^+_{SS} remains close to 70 Pa before to "suddenly" jumping towards another group characterized by $\sigma^+_{SS} \approx 10^3$ Pa when the shear rate exceeds $10^{-2}\,s^{-1}$.

On the other hand, the first normal stress difference exhibits non-monotonic variations of growing amplitude when the shear rate is increased. At low shear rates ($\dot{\gamma} \leq 3.2\ 10^{-3}\,s^{-1}$), N_1 first presents a plateau close to 0 Pa reminiscent of a quasi-linear regime before to become slightly negative when approaching the yield strain (close to $\gamma = 10^{-2}$ in Fig.3). At larger strain amplitude, the first normal stress difference increases quasi-monotonically before to saturate around $2\ 10^3$ Pa. Although it is qualitatively comparable, the situation becomes more interesting at higher shear rates ($\dot{\gamma} \geq 10^{-2}\,s^{-1}$) because the amplitude of the negative peak N_{1_p} becomes prominent, excluding any measurement artefacts. In these experiments, the strain onset of the negative N_1 peak is observed to match the shear stress build-up one (close to $\gamma = 10^{-1}$ in Fig. 4a), and not the "original" yield strain as further highlighted in Fig.5. Following the same logic, the position of the N_1 peak's minimum γ_p is then found to match the inflexion point of the shear stress build-up while its end seems to correspond to the stabilization of the shear stress. In between the peak minimum and the steady-state regime, N_1 also exhibits some sharp oscillations of moderated amplitude when $\dot{\gamma} \geq 3.2\ 10^{-1}\,s^{-1}$ (Fig.4b).

For the sake of clarity, the values of σ^+_{SS}, N_{1_p} and γ_p are reported in Fig.4c as a function of the shear rate. The comparison of these parameters extracted from start-up experiments makes very clear the transition in the range

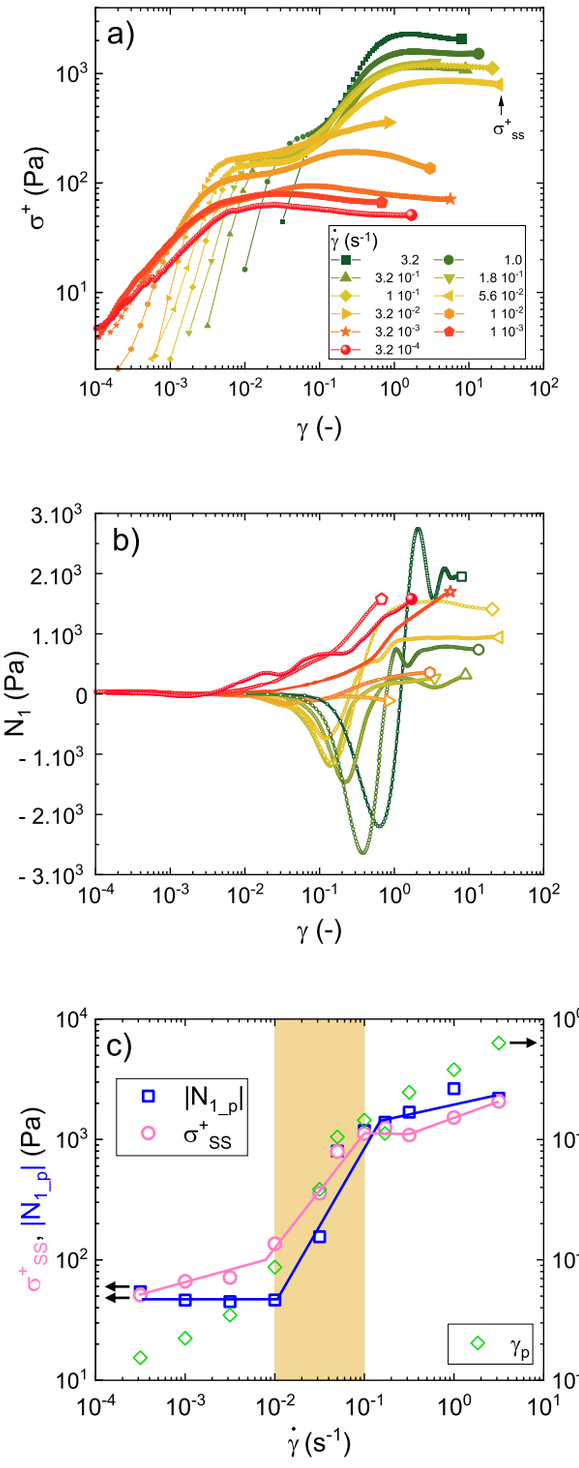

FIG. 4. a) Shear stress and b) First normal stress difference as a function of strain for different shear rates. σ^+ and N_1 curves are cut right before edge instabilities. c) Comparison of remarkable stress values during start-up tests highlighting a rheological transition between $10^{-2}\,s^{-1}$ and $10^{-1}\,s^{-1}$ (gold panel).

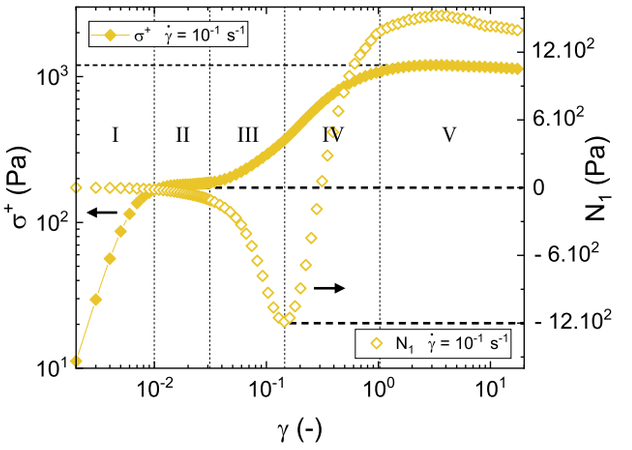

FIG. 5. Shear stress and first normal stress difference measured at $\dot{\gamma} = 10^{-1}\,s^{-1}$ during a start-up test. Roman numbers highlight the different structural regimes.

$10^{-2}\,s^{-1} < \dot{\gamma} < 10^{-1}\,s^{-1}$ and reveals the parallel trends of σ^+_{SS} and N_{1_p} with increasing the shear rate. To summarize: i) at low $\dot{\gamma}$, N_{1_p} is constant while σ^+_{SS} slightly increases; ii) in the transition zone, $|N_{1\_p}|$ and σ^+_{SS} both grow of ca. 1.5 decade. This transition is characterized by the apparition of a shear stress build-up (Fig.4a) and a pronounced first normal stress difference drop (Fig.4b); iii) at higher $\dot{\gamma}$, both N_{1_p} and σ^+_{SS} exhibit a pronounced slowdown of their growth. Anecdotally, γ_p exhibits a smoother evolution with the shear rate than the broken-line profiles of N_{1_p} and σ^+_{SS}.

To make it even clearer, we represent in Fig.5 both σ^+ and N_1 as a function of γ for $\dot{\gamma} = 10^{-1}\,s^{-1}$ where we assigned roman numbers (I-V) to the different regimes, each of them being associated to a 2D graphical representation in Fig.6. In here, the flow direction and the shear rate gradient are respectively along $\vec{x}_1$ and $\vec{x}_2$ resulting in a compression axis corresponding to the diagonal $\vec{x}_2 = -\vec{x}_1$ [47]. Note that in spite of our efforts to support the rheological data presented in Fig.4-5 with more advanced Rheo-SAXS experiments, no direct structural evidence of the 5-steps regime scenario presented below could be extracted. We discuss the technical difficulties in SM Section S-V.

Zone I corresponds to the quasi-linear regime where the shear stress progressively grows with the strain amplitude owing to the inter-particles interactions (tangential lines in Fig.6) storing a good part of the shear energy (see also dynamic frequency sweep tests in SM Section S-IV). Particles may be seen as located in cages formed by their neighbors that oppose to the flow. Because the solid loading is high, the yield strain amplitude is however quite low, corresponding to the end of this regime at $\gamma = 10^{-2}$.

Zone II represents the transition from the quasi-linear regime to the onset of the non-linear one. In this zone, the shear stress saturates at $\sigma^+ = 2\ 10^2$ Pa corresponding to the

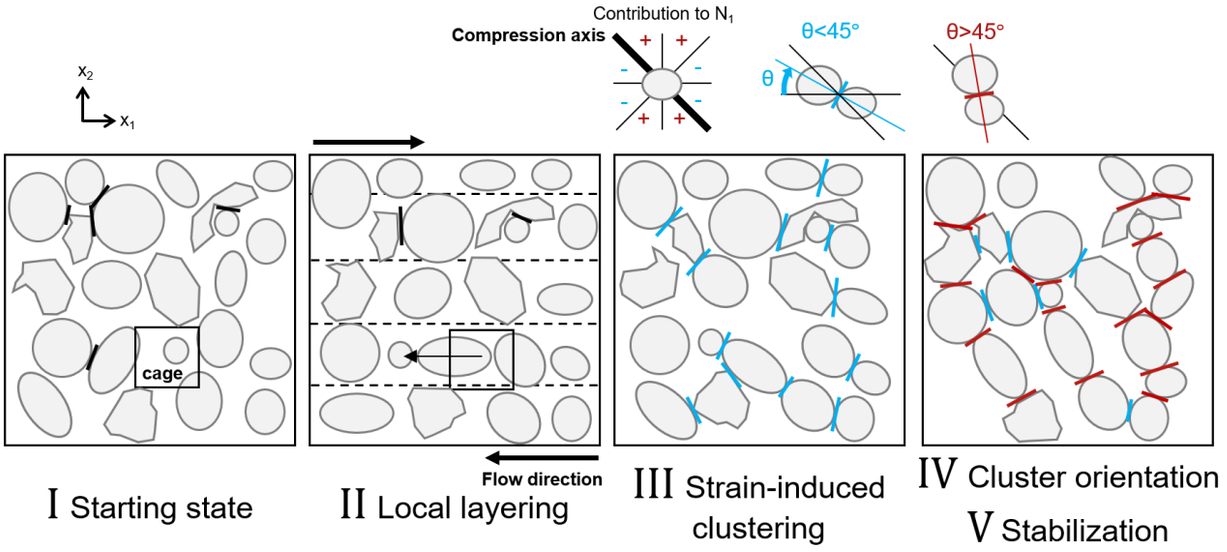

FIG. 6. Structural description of particles arrangement under steady shear at $\dot{\gamma} > 10^{-2}\,\mathrm{s}^{-1}$. Thick lines represent contact between particles. I) Quasi-linear regime, II) Local layering, III) Clustering at $\theta < 45°$ (negative N_1), IV) Clustering at $\theta > 45°$ (positive N_1).

rupture of the colloidal cages (yield stress) and the beginning of the local layering effect as illustrated in Fig.6 (II). Particles gain mobility and are less likely to store mechanical energy. While the first normal stress difference is still close to 0 Pa, it starts to decrease significantly prefiguring particles alignment at higher strain amplitude.

Zone III contemporaneously presents a strong increase of σ^+ and N_1 (in the negative direction) indicating a major structural transition. In particular, the diverging profile of σ^+ suggests a multiplication of the number of contacts per time unit, i.e., clustering, as already observed at intermediate shear rates by Koumakis et al.[48]. Besides, because the orientation of particles contacts defines their contribution to normal forces[49,50], $N_1 < 0$, corresponding to $\sigma_{22} < \sigma_{11}$, suggests therefore that clustering occurs preferentially along $\theta < 45°$. In other words, σ_{11} is increasingly negative while σ_{22} is decreasingly positive as particles contacts are promoted in the flow direction ($\vec{x_1}$).

Zone IV starts at the inflexion point of the σ^+ growth and the minimum of N_1. The transition from zone III to IV therefore marks a deceleration in the creation of new frictional contacts between the particles and a change in the orientation of the transient clusters. Focusing on N_1 actually suggests that the amplitude of σ_{11} and σ_{22} are now decreasing and increasing respectively until reaching $N_1 = 0$ and continuing up to a stable level at $N_1 = 1.3\ 10^3$ Pa. This result can be understood based on the progressive "rotation" of the clusters formation from $\theta < 45°$ to $\theta > 45°$, with $\theta = 45°$ corresponding to $N_1 = 0$, i.e., a symmetric situation with respect to the compression axis, where $\sigma_{11} = \sigma_{22}$.

Zone V finally indicates stabilized and positive maximal σ^+ and N_1 corresponding to a material steady state where the number of transient clusters and branches have reached an equilibrium. Large objects aligned preferentially along $\theta > 45°$ dominate the macroscopic rheological behavior without leading to jamming.

C. Relaxation

Post start-up relaxation measurements ($\sigma^-(t, \dot{\gamma} = 0\,\mathrm{s}^{-1})$) are presented in Fig.7a for the whole set of shear rates investigated in the previous section. While the data systematically exhibit an inverse sigmoid shape profile, they are characterized by quite different initial and final stress levels as well as different relaxation times. Regarding the latter point, two decreasing "monomodal" exponential functions were required to fit appropriately the data as follows

$$\sigma^-(t) = \sigma_\infty + \sigma_1^-\ exp(-t/\tau_1) + \sigma_2^-\ exp(-t/\tau_2) \quad (1)$$

where $t = 0\,\mathrm{s}$ is the beginning of the relaxation and $\sigma_\infty = \sigma^-(t = 10^2\,\mathrm{s})$. The shear stress values at $t = 0\,\mathrm{s}$ and $t = 10^2\,\mathrm{s}$ are reported in Fig.7b as a function of $\dot{\gamma}$. Similarly, relaxation times collected from the fitting procedure (see SM Section S-VI) are displayed in Fig.7c. Note that a close look at the data reveals a slight but systematic increase of σ^- at long time, we discuss this unexpected result in Appendix 1.

As expected, the two above-mentioned groups of experiments satisfying $\dot{\gamma} < 10^{-2}\,\mathrm{s}^{-1}$ on one hand, and $\dot{\gamma} > 10^{-2}\,\mathrm{s}^{-1}$ on the other hand, are well visible in Fig.7a. Interestingly, beyond the stress at $t = 0\,\mathrm{s}$, a clear distinction between the two groups also appears at long relaxation time where the residual stresses corresponding to steady-shear performed at $\dot{\gamma} > 10^{-2}\,\mathrm{s}^{-1}$ are significantly higher than the ones conducted at $\dot{\gamma} < 10^{-2}\,\mathrm{s}^{-1}$. The hatched areas reported in Fig.7a-b further highlight this observation, discriminating samples that experienced, or not, the structural transition occurring at $\dot{\gamma} > 10^{-2}\,\mathrm{s}^{-1}$.

Overall, it is worth mentioning that none of the samples achieve $\sigma_\infty = 0\,\mathrm{Pa}$, corroborating the systematic non-linear

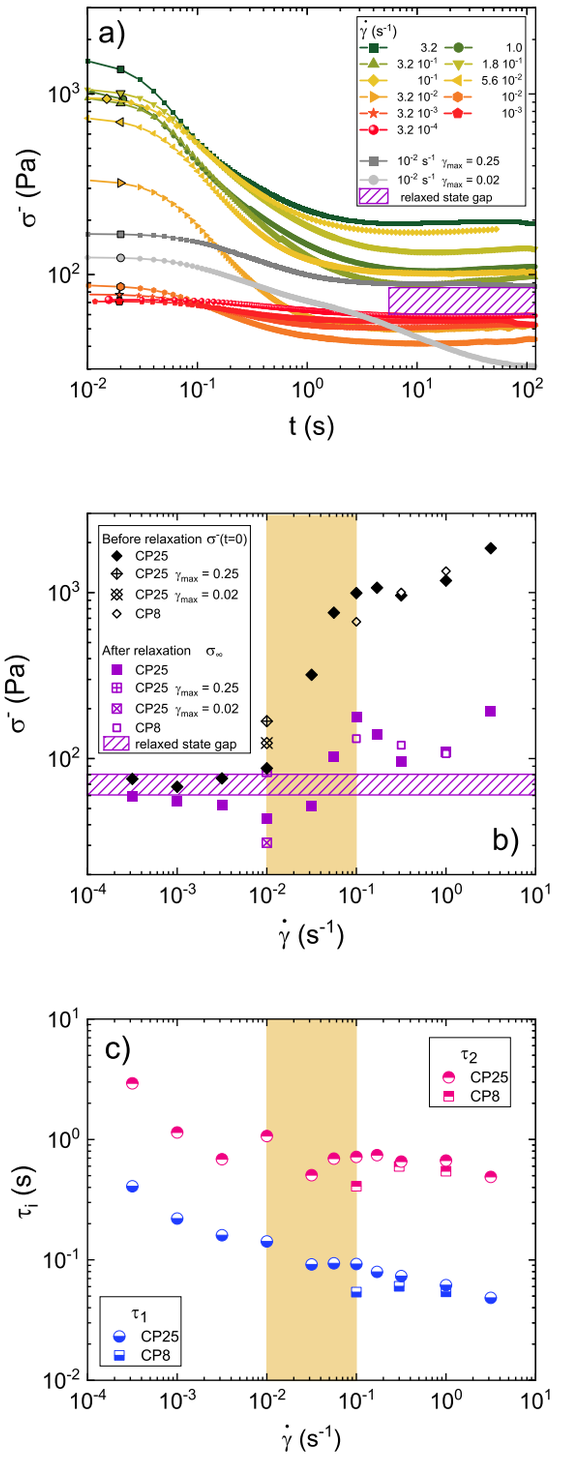

FIG. 7. a) Shear stress relaxation after start-up experiments. b) Shear stress measured before and after relaxation highlighting the structural transition between $10^{-2}\,s^{-1}$ and $10^{-1}\,s^{-1}$ (gold panel). c) Relaxation times obtained by fitting the relaxation data with two decreasing exponential functions (details are reported in SM section S-VI) (with gold panel).

nature of the experiments, including at the lowest shear rate of $\dot{\gamma} = 3.2\ 10^{-4}\,s^{-1}$. This result indicates a durable modification of the paste structure regardless of $\dot{\gamma}$, likely involving a certain degree of permanent clustering, which combined with the elastic properties of the paste ($G' > G''$, see SM Section S-VII), results in stress persistence as proposed by Corté et al.[26,51]. Of particular interest is the case of $\dot{\gamma} = 10^{-2}\,s^{-1}$ for which we repeated start-up experiments at two additional maximum strain amplitudes $\gamma_{max} = 0.02$ and 0.25, corresponding to the inflexion point and the top of the shear stress build-up in Fig.4a (see Appendix 2 for raw data). The two respective values of σ_∞ appear on both sides of the hatched area in Fig.7b indicating therefore that beyond the shear rate, the strain amplitude also controls the degree of persistent clustering. In fact, while shearing at $\dot{\gamma} = 10^{-2}\,s^{-1}$ up to $\gamma = 0.02$ leads to a stress relaxation that belongs to the first group of experiments (low value of σ_∞), pursuing the deformation up to $\gamma = 0.25$, i.e., beyond the shear stress build-up, results in a slower and less complete relaxation, reminiscent of the second group of experiments (high value of σ_∞). This result means that the residual stress at the end of the stress relaxation is not only a function of the shear rate (as reported by Moghimi et al.[52]), but also a function of the shear strain in agreement with Sudreau et al.[53].

The presence of the structural transition is less obvious when focusing on the relaxation times that present at first slight continuous and decreasing profiles when increasing the shear rate as presented in Fig.7c. Nevertheless, a significant break in slope is visible for τ_1 (and to a lesser extent for τ_2) at $\dot{\gamma} > 10^{-2}\,s^{-1}$, suggesting that the larger fraction of the stress accumulated into larger (and/or more numerous) clusters is able to relax quickly and independently of the shear rate above $\dot{\gamma} = 10^{2}\,s^{-1}$. In fact, although the origin of these two modes is not fully understood, we believe that their parallel trends suggest a similar physical origin that is the intra-cluster relaxation of the compressive stress.

The main qualitative result that emerges from start-up and relaxation experiments is thus that the application of a steady shear promotes the formation of both transient and durable clusters and that this effect is further enhanced when the shear rate is increased above $10^{-2}\,s^{-1}$. These observations are in sharp contrast with the work of Moghimi et al.[52] and Koumakis et al.[27] where the authors deal with monodisperse PMMA beads suspensions characterized by a particle radius of a few hundreds of nanometers and a solid loading of 44 vol %, representing a comparable situation to the present study. In these articles, the authors convincingly associate experiments and simulations to demonstrate that steady shear conversely tends to reduce the number of contacts between the PMMA spheres resulting in a growing homogeneity in the material for a higher Peclet number (i.e., a higher shear rate). Beyond similar particles radius and solid loading, this large discrepancy emphasizes therefore the importance of the inter-particle interactions and the particles geometry (smooth and monodisperse spheres vs. rough and polydisperse polyhedra), possibly resulting in interlocking events in the latter case. For the sake of completeness, it is worth mentioning that our linear dynamic moduli are ca.10^2 times higher than in the

above-mentioned works and present a thrice as lower loss factor that expectedly modifies dramatically non-linear effects. Another relevant case is that treated by Moghimi et al. in a different publication[54] where the authors reported the possibility to re-aggregate or re-homogenize their PMMA beads by applying an oscillatory shear of moderate or large amplitude respectively. Contrarily, Corté et al. developed a theoretical model predicting the progressive deagglomeration of colloids for moderate (but repeated) oscillatory shear solicitations[26]. (We show the impact of non-linear oscillatory versus steady shear on our paste in SM Section S-VII).
To sum up, the reader must keep in mind that beyond the shape of the strain signal (oscillatory vs. steady), the amplitude of the deformation is a key factor in tuning the structure of colloidal suspensions and that the final result mostly depends on the nature of the interparticle interactions as well as the particles shape when non-spherical objects are considered. In the next section, we show how we can manipulate the steady shear viscosity of 3Y-F01 SLA paste by using orthogonal rheometry methods.

D. Orthogonal superposition rheometry

1. *Flow curves*

Guided by our will to avoid shear-thinning interruption to enhance the SLA paste process, we present in this last section orthogonal rheometry experiments where we apply a vertical oscillatory strain while shearing the paste with a double-wall Couette geometry from high to low shear rates. The first results presented in Fig. 8a, consist of a series of flow curves where we systematically vary the frequency ($\omega_\perp$) and the amplitude (ε) of the vertical strain. At first sight, it appears that the application of the vertical solicitation globally lowers the viscosity profile, strongly mitigating the shear-thinning cessation observed between $\dot{\gamma} = 10^{-2}\,\mathrm{s}^{-1}$ and $10^{-1}\,\mathrm{s}^{-1}$ so far. A closer look at these data shows that while the paste viscosity at high shear rate ($\dot{\gamma} > 2\,\mathrm{s}^{-1}$) remains essentially unchanged, it is significantly lowered in presence of a vertical strain at lower shear rate, with the critical value between these two regimes ($\dot{\gamma}_c$) increasing with higher $\omega_\perp$ and ε. This effect is further highlighted in Fig.8b where the shear viscosity in presence of a vertical strain is normalized by the "classic" flow curve ($\varepsilon = 0$). This representation makes clearly emerge that the higher $\omega_\perp$, the higher the shear rate at which the OSP flow curve diverges from the classic one. The variation of $\dot{\gamma}_c$ as a function of $\omega_\perp$ is reported in the inset of Fig.8b, indicating a power law dependence following $\dot{\gamma}_c \propto \omega_\perp^{0.81}$. As one may have anticipated, it is also worth noting that decreasing the amplitude of the vertical oscillation by a factor 10 ($\varepsilon = 5\ 10^{-3}$ instead of $5\ 10^{-2}$) while keeping the same frequency ($\omega_\perp = 100\,\mathrm{rd\,s}^{-1}$) results in a much lower impact on the shear viscosity. Here, a rescaling invoking the maximum strain rate $\dot{\varepsilon}_{max} = \omega_\perp \varepsilon$ instead of $\omega_\perp$ does not seem to be relevant, suggesting a threshold effect of the vertical strain amplitude rather than a continuous variation of $\dot{\gamma}_c$ with the maximum strain rate experienced by the paste.

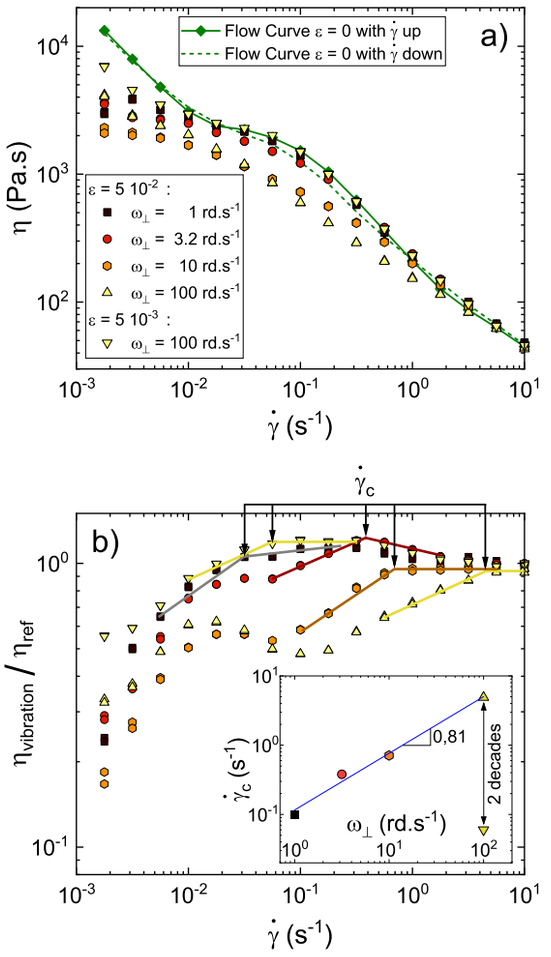

FIG. 8. a) Flow curves measured with constant orthogonal oscillatory vibration of different parameters compared with standard flow curve. Inset of viscosity multiplied by shear rate at exponent $\alpha = 0.57$ in function of shear rate to track the evolution of the flow curve bump with vibration b) Ratio of vibrated sample viscosity normalized by reference flow curve viscosity in function of shear rate with tangential interpolation to localize the shear rate at which flow curve is no longer influenced by vibration. Inset graph of shear rate of vibration influence limit in function of vibration frequency.

We want to emphasize that these results are in excellent qualitative agreement with previous works by Hanotin et al.[55–57], Wortel et al.[58] and Garat et al.[59], where the authors demonstrated a similar fluidization effect in dense non-colloidal suspensions based on Newtonian liquids as well as in granular media. In particular, by using a stress-controlled rheometer equipped with a powder cell connected to a vibration shaker, Hanotin et al. emphasized that the terminal relaxation time of their monodisperse micronic spheres suspensions could be reduced by ca. two decades in presence of a vibrational stress of lower amplitude than the "static" yield stress of the material[55]. These measurements were then convincingly supported by light scattering experiments (DWS)

showing that the particles diffusion was correspondingly accelerated by the same quantity[56]. We also refer the reader to Fig. 3 in ref.[57] for a direct comparison with our Fig. 8a, the sole difference being the stress-controlled nature of the experiment. Using the same apparatus, Garat et al.[59] also evidenced the transition from a solid-like to a liquid-like behavior in presence of a vibrational stress, making the yield stress of their dense suspension of micronic rough silica vanishing, being qualitatively similar to what is visible in our Fig. 8a at low $\dot{\gamma}$ and high $\omega_\perp$ (non-divergent viscosity).

Overall, it appears that superposing vertical vibrations to the shear flow accelerates the dynamics of our nanoparticles-based SLA paste by perturbing the formation of the transient clusters from intermediate shear rates. The corresponding reduction of viscosity is dependant on the vibration characteristics, which above a certain amplitude threshold provides an onset of the viscosity loss ($\dot{\gamma}_c$) evolving almost linearly with the frequency of the vertical solicitation ($\omega_\perp$). To avoid confusion on the interest of the oscillatory solicitation for the SLA process, it is here important to remind the reader that the effective shear rate experienced by the paste during the scraping ($\dot{\gamma}_{SLA} \approx 10^2\,\mathrm{s}^{-1}$) is much higher than the range in which a visible effect on the viscosity is reported in Fig.8. Yet, the application of a continuous vibration (in the shear plane) while scraping was observed to significantly enhance the surface quality of the paste layers[38]. This result suggests therefore that beyond the very moment at which the paste is sheared, corresponding to its passage under the scraping blade, the vibration is likely to help the shape recovery (and stress relaxation) of the material right after the blade is passed. Moreover, oscillatory strain is also very likely to help to reduce the adhesion of the paste on the back of the scraper, which is another common issue encountered when dealing with SLA.

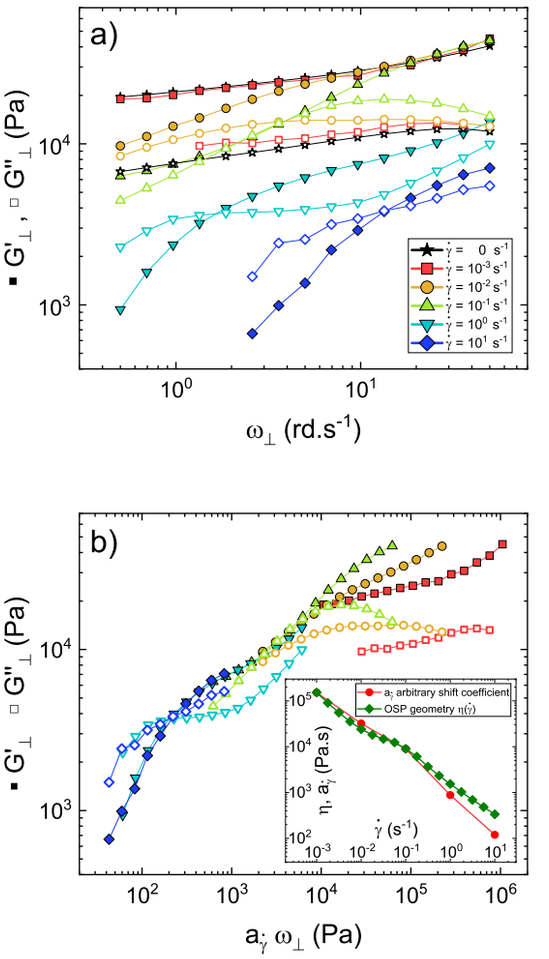

FIG. 9. a) Vertical direction dynamic frequency sweep performed at $\varepsilon = 3\ 10^{-3}$ while steady shear is running at different shear rates. b) Frequency sweep results shifted by coefficient $a_{\dot{\gamma}}$ to test master curve in the case of viscosity time superposition. Inset: overlap of the $a_{\dot{\gamma}}$ coefficient and the viscosity as a function of the shear rate to evaluate the superposition hypothesis.

2. *Orthogonal dynamic frequency sweeps*

For the sake of completeness and to provide a deeper understanding of the effect of the vertical oscillatory strain on the (time-dependent) properties of the paste, we present in Fig.9a orthogonal dynamic frequency sweeps of steady sheared paste from $\dot{\gamma} = 0\,\mathrm{s}^{-1}$ up to $\dot{\gamma} = 10^1\,\mathrm{s}^{-1}$. At rest ($\dot{\gamma} = 0\,\mathrm{s}^{-1}$), the paste response is gel-like with both dynamic moduli (G' and G'') slightly increasing with the frequency and an almost constant loss factor. The G' plateau is close to $2\ 10^4$ Pa - $3\ 10^4$ Pa, in good agreement with "classic" dynamic frequency sweep tests reported in SM Section S-IV, in spite of the difficult setup of the OSP experiments owing to the yield stress fluid nature of the SLA paste. While setting the shear rate at $\dot{\gamma} = 10^{-3}\,\mathrm{s}^{-1}$ provides an almost unchanged response of the material, increasing its value to $\dot{\gamma} = 10^{-2}\,\mathrm{s}^{-1}$ clearly accelerates the paste relaxation. In fact, G'' is significantly higher and presents a slight bell-shape profile on the whole frequency range while G' drops for $\omega_\perp < 4\,\mathrm{rd\,s}^{-1}$. These effects become even more visible at $\dot{\gamma} = 10^{-1}\,\mathrm{s}^{-1}$ where a G', G'' crossover appears at $\omega_\perp = 3\,\mathrm{rd\,s}^{-1}$, marking the transition from a solid-like to liquid-like behavior. For higher shear rates ($\dot{\gamma} = 1\,\mathrm{s}^{-1}$ and $10^1\,\mathrm{s}^{-1}$), the dynamic moduli are clearly weaker, exhibiting a viscoelastic liquid relaxation profile. Both the characteristic exponents increase up to ≈ 1 and the crossover eventually shifts to higher frequency, reminiscent of the shear-thinning effect caused by a higher shear rate. These observations are qualitatively similar to the ones reported by Jacob et al.[60] on the fluidization of model dense suspensions of star-like micelles. In that paper, the authors further demonstrated that the position of the G', G'' crossover (ω_c) varied in a sublinear way with the shear rate such as $\omega_c \propto \dot{\gamma}^{0.8}$ whereas hard-spheres were characterized by a linear dependency[61], in agreement with our results at $\dot{\gamma} = 1\,\mathrm{s}^{-1}$ and $10^1\,\mathrm{s}^{-1}$ respectively providing $\omega_c = 1.3\,\mathrm{rd\,s}^{-1}$ and $1.2\ 10^1\,\mathrm{rd\,s}^{-1}$.

Following the idea of a time - shear rate superposition (TSS) principle such as emphasized in refs.[61–63], we provide in Fig.9b a tentative mastercurve where the G' and G'' data have been shifted horizontally by an arbitrary factor $a_{\dot{\gamma}}$, using

as a reference the measurement performed at $\dot{\gamma} = 10^{-1}\,\mathrm{s}^{-1}$ that we multiplied by $a_{\dot{\gamma}} = \eta(\dot{\gamma} = 10^{-1}\,\mathrm{s}^{-1})$ (see inset of Fig.9b). While the rest of the data could have been shifted in a similar way, i.e., using the corresponding steady shear viscosity as a shift factor, the resulting mastercurve was not satisfying from a graphical point of view so we preferred to apply a manual (and arbitrary) $a_{\dot{\gamma}}$ and compare it in a systematic way with the corresponding η value in Fig.9c. This representation illustrates well the quantitative similarity of the η and $a_{\dot{\gamma}}$ variations, confirming that a partial TSS principle stands. In fact, focusing on the high frequency range (Fig.9b) reveals nevertheless an important failure of the TSS, similarly as in ref.[62], where Moghimi et al. assigned it to some degree of structural anisotropy inducing different in-cage (rapid) dynamics. This idea actually seems in line with the presence of aligned clustering from $\dot{\gamma} > 10^{-2}\,\mathrm{s}^{-1}$ as evidenced in the previous section. At higher shear rate, the clusters are expected to be stronger and/or more numerous leading to higher dynamic moduli that will persist longer (until lower $\omega_{\perp}$). We believe that this effect is particularly strong in our case because of the pronounced polydispersity of our particles, both in terms of size and shape (that also include polyhedral geometries).

IV. CONCLUSIONS

We investigated the rheological properties of a commercial stereolithography (SLA) paste loaded with $\Phi = 49$ vol % of ZrO_2 sub-micronic particles in a systematic way by means of flow curves, start-up experiments and orthogonal rheometry. Flow curves first revealed an important interruption of the shear-thinning effect between $\dot{\gamma} = 10^{-2}\,\mathrm{s}^{-1}$ and $10^{-1}\,\mathrm{s}^{-1}$ suggesting the presence of a structural transition likely to impact negatively the scraping step of the SLA process, eventually resulting in major defects within the solid ceramic parts. Focusing on the transient viscosity, we have then emphasized a strong upturn of the shear stress occurring well after the usual yield point combined with a non-monotonic variation of the first normal stress difference, both effects becoming stronger with increasing the shear rate above $\dot{\gamma} = 10^{-2}\,\mathrm{s}^{-1}$. Subsequent relaxation tests characterized by two distinct modes have demonstrated the presence of residual stress in all the experiments, showing however a clear distinction between samples that experienced the structural transition ($\dot{\gamma} > 10^{-2}\,\mathrm{s}^{-1}$ - larger residual stress) or not ($\dot{\gamma} < 10^{-2}\,\mathrm{s}^{-1}$ - lower residual stress). This result obtained with a rheometer, suggests therefore that a considerable amount of mechanical stress is stored within the paste after the scraping step typically occurring at $\dot{\gamma}_{SLA} \approx 10^{2}\,\mathrm{s}^{-1}$ and that technical refinements could be proposed to improve the procedure. This question is at the heart of the last part of our article where we have used orthogonal superposition rheometry to demonstrate that oscillatory solicitations of minor amplitude are likely to play an important role in the "spreadability" of SLA pastes. In fact, we have shown that measuring flow curves under an orthogonal oscillatory strain enables to reduce (if not suppress) the abovementioned shear-thinning interruption, supporting the use of a vibrating blade in the SLA process. Beyond its technological interest, orthogonal rheometry further demonstrates here that the fluidization effect reported on model systems made of monodisperse hard colloids or soft micelles also occurs in SLA pastes containing very polydisperse (in size and shape) inorganic particles and that the time - shear rate superposition principle holds at low frequency. Perspectives of this work mainly concern the systematic study of the paste formulation and its impact on the transient rheology with the hope of controlling both dynamical and permanent clustering effects under high steady shear. Studying the adhesion of the paste to the blade by tack tests is also planned in order to rationalize and better identify another important aspect of the SLA printing process. Rheo-SAXS experiments conducted with an appropriate setup serving to verify the structural scenario presented in Fig.6 would also represent a major step forward.

SUPPLEMENTARY MATERIAL

Check for wall-slip effects (S-I), paste rest after conditioning (S-II) experimental details regarding the orthogonal superposition setup (S-III), dynamic frequency sweep tests prior to non linear solicitation (S-IV), rheo-SAXS results and related discussion (S-V), fitting of stress relaxation experiments (S-VI), dynamic strain sweep tests justifying the samples preparation (S-VII), symbol table (S-VIII).

ACKNOWLEDGMENTS

We wish to acknowledge the support of ID02 beamline team at ESRF, especially the local contact W. Chèvremont and the beamline manager T. Narayanan. (proposal MA-5093). Special thanks to CLyM platform (Lyon, France) for the use of their facilities. This work has been partly funded by a public grant from the French National Research Agency (ANR) under the “France 2030” investment plan, which has the reference EUR MANUTECH SLEIGHT - ANR-17-EURE-0026.

APPENDIX 1: NON-MONOTONIC BEHAVIOR AT LONG TIME

A close look at the data presented in Fig.7a in the last stages of the relaxation ($t > 1\ s$) reveals an unexpected, yet reproducible and systematic, stress upturn. This observation is even clearer in Fig.10 below where we normalized the data by $\sigma^-(t = 1\ s)$ to magnify the effect. This phenomenon was also observed by Hendricks et al.[64] in three different supramolecular systems made of i) EHUT bis-urea monomers based organogels, ii) semi-diluted long sticky-polymer solution and iii) very diluted polymer mixture solution in presence of NaOH. The authors rationalized the stress growth during relaxation by a phenomenological model accounting for the heterogeneous redistribution of energy implying the formation of partly aligned deformed domains. This concept is actually well in-line with the formation of anisotropic clusters during the stress "build-up" step as presented in Fig.5-6 (zones III and IV). Similarly as reported by Sudreau et al.[53], this important result confirms therefore that attractive colloidal systems can present similar features to associative polymer networks regarding non-monotonic stress relaxation.

Interestingly, the only exceptions to this trend are the data measured after start-up experiments performed up to much lower strain amplitudes, i.e., $\gamma_{max} = 0.02$ (light grey) and to a lesser extent, $\gamma_{max} = 0.25$ (dark grey) - see Appendix 2. These observations support the idea that a certain level of deformation is required to form the aligned domains and that their absence unavoidably leads to a conventionally decreasing (and monotonic) stress relaxation. Note that we cannot exclude that the structural change at the origin of this stress upturn during relaxation may be related to the thixotropic nature of the paste that is a frequent concern in this type of materials.[3,11,65–67] Note that longer relaxation tests and a more systematic variation of γ_{max} may have better illustrated this phenomenon that will undoubtedly deserve a particular attention in the future.

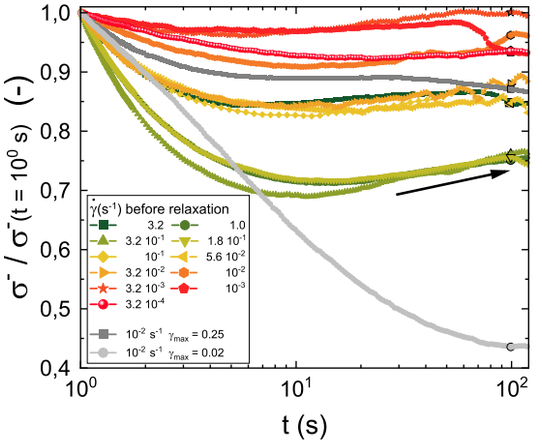

FIG. 10. Post start-up shear stress relaxation normalized by $\sigma^-(t = 1\,\mathrm{s})$ exhibiting a stress upturn at long relaxation time. The black arrow emphasizes the upturn.

APPENDIX 2: START-UP EXPERIMENTS AT $10^{-2}\,\mathrm{S}^{-1}$

The start-up experiment conducted at $\dot{\gamma} = 10^{-2}\,\mathrm{s}^{-1}$ exhibits a shear stress "bump" rather than a true and stable "build-up" as observed at higher shear rates (see Fig.4a). This observation suggests therefore that the formation of high-angle clusters ($\theta > 45°$), from $\gamma = 10^{-1}$ is not stable and that $\dot{\gamma} = 10^{-2}\,\mathrm{s}^{-1}$ represents a physical limit between two rheological regimes (low-angle vs. high-angle clustering). To deepen our understanding of the situation, we performed two additional start-up experiments consisting of a similar procedure with the sole difference being that they were stopped at a lower maximal strain ($\gamma_{max} = 0.02$ and 0.25), see Fig.11. The shear stress data are very similar in the three experiments confirming therefore the reproducibility of our methodology and the presence of the stress "bump". On the other hand, N_1 measurements exhibit more variability but they follow the same qualitative variations consisting of two successive negative peaks (denoted * and **) followed by a strong positive N_1 growth at large strain values.

While the first peak (*) is located at the end of the first shear stress increase ($\gamma \approx 10^{-2}$, corresponding to the yield stress of the paste), the second (**) is undoubtedly related to the apparent structural build-up as it happens at the strain corresponding to the shear stress bump ($\gamma \approx 10^{-1}$). One can remark that N_1 measurements follow similar trends but are not superimposed. We believe that the metastable nature of the transition (bump) at $\dot{\gamma} = 10^{-2}\,\mathrm{s}^{-1}$ tends to reduce the measurement reproducibility. Noteworthy is the fact that the coexistence of the two N_1 peaks is not visible at higher shear rates, probably because of the fact that the second peak (of larger amplitude) masks the first one.

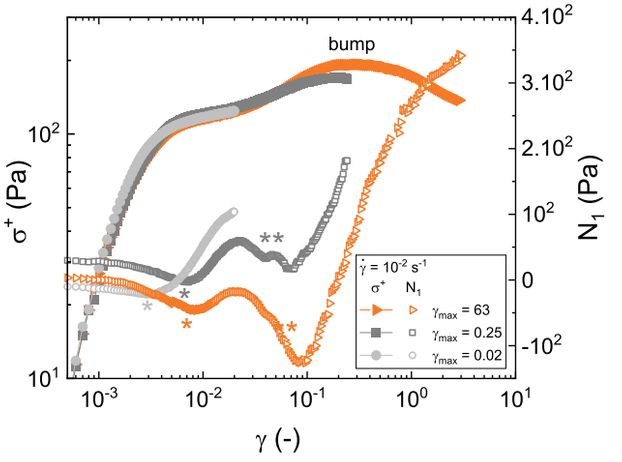

FIG. 11. Shear stress and first normal stress difference as a function of the strain for start-up experiments conducted at $\dot{\gamma} = 10^{-2}\,\mathrm{s}^{-1}$ and up to $\gamma_{max} = 63$, 0.25 and 0.02. Singular maxima in the first normal stress difference are emphasized with * and ** symbols.

REFERENCES

[1]E. García-Tuñón, R. Agrawal, B. Ling, and D. Dennis, "Fourier-transform rheology and printability maps of complex fluids for three-dimensional printing," Physics of Fluids **35**, 017113 (2023).
[2]A. G. Hasib, S. Niauzorau, W. Xu, S. Niverty, N. Kublik, J. Williams, N. Chawla, K. Song, and B. Azeredo, "Rheology scaling of spherical metal powders dispersed in thermoplastics and its correlation to the extrudability of filaments for 3d printing," Additive Manufacturing **41**, 101967 (2021).
[3]L. del Mazo-Barbara and M.-P. Ginebra, "Rheological characterisation of ceramic inks for 3d direct ink writing: A review," Journal of the European Ceramic Society **41**, 18–33 (2021).
[4]J. A. Lewis, J. E. Smay, J. Stuecker, and J. Cesarano, "Direct ink writing of three-dimensional ceramic structures," Journal of the American Ceramic Society **89**, 3599–3609 (2006).
[5]P. Veteška, Z. Hajdúchová, J. Feranc, K. Tomanová, J. Milde, M. Kritikos, Ľuboš Bača, and M. Janek, "Novel composite filament usable in low-cost 3d printers for fabrication of complex ceramic shapes," Applied Materials Today **22**, 100949 (2021).
[6]M. Schwentenwein and J. Homa, "Additive manufacturing of dense alumina ceramics," International Journal of Applied Ceramic Technology **12**, 1–7 (2015).
[7]D. W. Rosen, "Stereolithography and rapid prototyping," in BioNanoFluidic MEMS, edited by P. J. Hesketh (Springer US, Boston, MA, 2008) pp. 175–196.
[8]J. W. Halloran, "Ceramic stereolithography: Additive manufacturing for ceramics by photopolymerization," Annual Review of Materials Research **46**, 19–40 (2016).
[9]C. Chaput, T. Chartier, and F. Doreau, "Method and composition for making ceramic parts by stereolithography and use in dentistry," (2003), wO 03/066326 A2.
[10]Y. Zhang, Q. Zhang, F. He, F. Zuo, and X. Shi, "Fabrication of cancellous-bone-mimicking beta-tricalcium phosphate bioceramic scaffolds with tunable architecture and mechanical strength by stereolithography 3d printing," Journal of the European Ceramic Society **42**, 6713–6720 (2022).
[11]J. Nie, M. Li, W. Liu, W. Li, and Z. Xing, "The role of plasticizer in optimizing the rheological behavior of ceramic pastes intended for stereolithography-based additive manufacturing," Journal of the European Ceramic Society **41**, 646–654 (2021).
[12]A. Goswami, A. K, N. Balashanmugam, A. M. Umarji, and G. Madras, "Optimization of rheological properties of photopolymerizable alumina suspensions for ceramic microstereolithography," Ceramics International **40**, 3655–3665 (2014).
[13]T. Chartier, A. Badev, Y. Abouliatim, P. Lebaudy, and L. Lecamp, "Stereolithography process: Influence of the rheology of silica suspensions and of the medium on polymerization kinetics – cured depth and width," Journal of the European Ceramic Society **32**, 1625–1634 (2012).
[14]W. Liu, M. Li, J. Nie, C. Wang, W. Li, and Z. Xing, "Synergy of solid loading and printability of ceramic paste for optimized properties of alumina via stereolithography-based 3d printing," Journal of Materials Research and Technology **9**, 11476–11483 (2020).
[15]M. Maillard, Imprimabilité de pâtes céramiques par robocasting, Ph.D. thesis, Université de Lyon (2022).
[16]M. Maillard, J. Chevalier, L. Gremillard, G. P. Baeza, E.-J. Courtial, S. Marion, and V. Garnier, "Optimization of mechanical properties of robocast alumina parts through control of the paste rheology," Journal of the European Ceramic Society **43**, 2805–2817 (2023), 17th European Inter-Regional Conference on Ceramics.
[17]J. Piette, A. A. Moud, J. Poisson, B. Derakhshandeh, Z. M. Hudson, and S. G. Hatzikiriakos, "Rheology of mature fine tailings," Physics of Fluids **34**, 063104 (2022).
[18]A. Malmir, J. H. Piette, B. Derakhshandeh, D. Sztukowski, and S. G. Hatzikiriakos, "On the thixotropy of mature fine tailings," Physics of Fluids **35**, 063103 (2023).
[19]F. Giustozzi, K. Mansour, F. Patti, M. Pannirselvam, and F. Fiori, "Shear rheology and microstructure of mining material-bitumen composites as filler replacement in asphalt mastics," Construction and Building Materials **171**, 726–735 (2018).
[20]J. Mewis and N. J. Wagner, "Non-spherical particles," in Colloidal Suspension Rheology, Cambridge Series in Chemical Engineering (Cambridge University Press, 2011) p. 155–179.
[21]J. Sun, J. Binner, and J. Bai, "Effect of surface treatment on the dispersion of nano zirconia particles in non-aqueous suspensions for stereolithography," Journal of the European Ceramic Society **39**, 1660–1667 (2019).
[22]K. N. Pham, G. Petekidis, D. Vlassopoulos, S. U. Egelhaaf, P. N. Pusey, and W. C. K. Poon, "Yielding of colloidal glasses," Europhysics Letters **75**, 624 (2006).
[23]K. N. Pham, G. Petekidis, D. Vlassopoulos, S. U. Egelhaaf, W. C. K. Poon, and P. N. Pusey, "Yielding behavior of repulsion- and attraction-dominated colloidal glasses," Journal of Rheology **52**, 649–676 (2008).
[24]N. Koumakis, P. Ballesta, R. Besseling, W. C. K. Poon, J. F. Brady, and G. Petekidis, "Colloidal gels under shear: Strain rate effects," AIP Conference Proceedings **1518**, 365–371 (2013).
[25]S. Jamali, A. Boromand, N. Wagner, and J. Maia, "Microstructure and rheology of soft to rigid shear-thickening colloidal suspensions," Journal of Rheology **59**, 1377–1395 (2015).
[26]L. Corté, P. M. Chaikin, J. P. Gollub, and D. J. Pine, "Random organization in periodically driven systems," Nature Physics **4**, 420–424 (2008).
[27]N. Koumakis, E. Moghimi, R. Besseling, W. C. K. Poon, J. F. Brady, and G. Petekidis, "Tuning colloidal gels by shear," Soft Matter **11**, 4640–4648 (2015).
[28]L. Lobry, E. Lemaire, F. Blanc, S. Gallier, and F. Peters, "Shear thinning in non-brownian suspensions explained by variable friction between particles," Journal of Fluid Mechanics **860**, 682–710 (2019).
[29]R. Seto, R. Botet, M. Meireles, G. K. Auernhammer, and B. Cabane, "Compressive consolidation of strongly aggregated particle gels," Journal of Rheology **57**, 1347–1366 (2013).
[30]R. Mari, R. Seto, J. F. Morris, and M. M. Denn, "Shear thickening, frictionless and frictional rheologies in non-brownian suspensions," Journal of Rheology **58**, 1693–1724 (2014).
[31]J. F. Morris, "Lubricated-to-frictional shear thickening scenario in dense suspensions," Phys. Rev. Fluids **3**, 110508 (2018).
[32]J. F. Morris, "Shear thickening of concentrated suspensions: Recent developments and relation to other phenomena," Annual Review of Fluid Mechanics **52**, 121–144 (2020).
[33]N. J. Wagner and J. F. Brady, "Shear thickening in colloidal dispersions," Physics Today **62**, 27–32 (2009).
[34]A. Singh, C. Ness, R. Seto, J. J. de Pablo, and H. M. Jaeger, "Shear thickening and jamming of dense suspensions: The "roll" of friction," Phys. Rev. Lett. **124**, 248005 (2020).
[35]N. Malbranche, A. Santra, B. Chakraborty, and J. Morris, "Scaling analysis of shear thickening suspensions," Frontiers in Physics **10**, 946221 (2022).
[36]S. Pradeep, M. Nabizadeh, A. R. Jacob, S. Jamali, and L. C. Hsiao, "Jamming distance dictates colloidal shear thickening," Phys. Rev. Lett. **127**, 158002 (2021).
[37]S. Pradeep and L. C. Hsiao, "Contact criterion for suspensions of smooth and rough colloids," Soft Matter **16**, 4980–4989 (2020).
[38]V. Pateloup, V. Michaud, and T. Chartier, "Optimization of part orientation and adapted supports for manufacturing of ceramic parts by stereolithography using finite element simulations," Open Ceramics **6**, 100132 (2021).
[39]T. Schweizer, "Measurement of the first and second normal stress differences in a polystyrene melt with a cone and partitioned plate tool," Rheologica Acta **41**, 337–344 (2002).
[40]D. C. Venerus and H. Kahvand, "Normal stress relaxation in reversing double-step strain flowsa)," Journal of Rheology **38**, 1297–1315 (1994).
[41]S. Costanzo, Q. Huang, G. Ianniruberto, G. Marrucci, O. Hassager, and D. Vlassopoulos, "Shear and extensional rheology of polystyrene melts and solutions with the same number of entanglements," Macromolecules **49**, 3925–3935 (2016).
[42]R. Tao and A. M. Forster, "End effect correction for orthogonal small strain oscillatory shear in a rotational shear rheometer," Rheologica Acta **59**, 95–108 (2020).
[43]A. Franck, "Orthogonal superposition on the ares-g2," TA instruments, application note, APN035 (2013).
[44]T. Zemb and P. Lindner, Neutron, X-rays and light. Scattering methods applied to soft cond (North Holland, 2002) Chap. 3. General Theorems in Small-Angle Scattering, O.Spalla, pp. 49–71.
[45]G. P. Baeza, A.-C. Genix, C. Degrandcourt, L. Petitjean, J. Gummel, M. Couty, and J. Oberdisse, "Multiscale filler structure in simplified in-

dustrial nanocomposite silica/sbr systems studied by saxs and tem," Macromolecules **46**, 317–329 (2013).
[46]R. J. E. Andrade, A. R. Jacob, F. J. Galindo-Rosales, L. Campo-Deaño, Q. Huang, O. Hassager, and G. Petekidis, "Dilatancy in dense suspensions of model hard-sphere-like colloids under shear and extensional flow," Journal of Rheology **64**, 1179–1196 (2020).
[47]R. Seto, A. Singh, B. Chakraborty, M. M. Denn, and J. F. Morris, "Shear jamming and fragility in dense suspensions," Granular Matter **21**, 82 (2019).
[48]N. Koumakis and G. Petekidis, "Two step yielding in attractive colloids: transition from gels to attractive glasses," Soft Matter **7**, 2456–2470 (2011).
[49]D. R. Foss and J. F. Brady, "Structure, diffusion and rheology of brownian suspensions by stokesian dynamics simulation," Journal of Fluid Mechanics **407**, 167–200 (2000).
[50]M. M. Denn and J. F. Morris, "Rheology of non-brownian suspensions," Annual Review of Chemical and Biomolecular Engineering **5**, 203–228 (2014).
[51]L. Corté, S. J. Gerbode, W. Man, and D. J. Pine, "Self-organized criticality in sheared suspensions," Phys. Rev. Lett. **103**, 248301 (2009).
[52]E. Moghimi, A. R. Jacob, and G. Petekidis, "Residual stresses in colloidal gels," Soft Matter **13**, 7824–7833 (2017).
[53]I. Sudreau, M. Auxois, M. Servel, E. Lécolier, S. Manneville, and T. Divoux, "Residual stresses and shear-induced overaging in boehmite gels," Phys. Rev. Mater. **6**, L042601 (2022).
[54]E. Moghimi, A. Jacob, N. Koumakis, and G. Petekidis, "Colloidal gels tuned by oscillatory shear," Soft Matter **13**, 2371 (2017).
[55]C. Hanotin, S. K. De Richter, P. Marchal, L. J. Michot, and C. Baravian, "Vibration-induced liquefaction of granular suspensions," Physical review letters **108**, 198301 (2012).
[56]C. Hanotin, P. Marchal, L. J. Michot, C. Baravian, and S. K. de Richter, "Dynamics of vibrated granular suspensions probed by mechanical spectroscopy and diffusing wave spectroscopy measurements," Soft Matter **9**, 9352–9360 (2013).
[57]C. Hanotin, S. Kiesgen de Richter, L. Michot, and P. Marchal, "Viscoelasticity of vibrated granular suspensions," Journal of Rheology **59**, 253–273 (2015).
[58]G. Wortel, O. Dauchot, and M. van Hecke, "Criticality in vibrated frictional flows at a finite strain rate," Physical review letters **117**, 198002 (2016).
[59]C. Garat, S. Kiesgen de Richter, P. Lidon, A. Colin, and G. Ovarlez, "Using good vibrations: Melting and controlled shear jamming of dense granular suspensions," Journal of Rheology **66**, 237–256 (2022).
[60]A. Jacob, A. Poulos, A. Semenov, J. Vermant, and G. Petekidis, "Flow dynamics of concentrated starlike micelles: A superposition rheometry investigation into relaxation mechanisms," Journal of Rheology **63**, 641–653 (2019).
[61]A. R. Jacob, A. S. Poulos, S. Kim, J. Vermant, and G. Petekidis, "Convective cage release in model colloidal glasses," Physical Review Letters **115**, 218301 (2015).
[62]E. Moghimi, J. Vermant, and G. Petekidis, "Orthogonal superposition rheometry of model colloidal glasses with short-ranged attractions," Journal of Rheology **63**, 533–546 (2019).
[63]S. H. Sung, S. Kim, J. Hendricks, C. Clasen, and K. H. Ahn, "Orthogonal superposition rheometry of colloidal gels: time-shear rate superposition," Soft Matter **14**, 8651–8659 (2018).
[64]J. Hendricks, A. Louhichi, V. Metri, R. Fournier, N. Reddy, L. Bouteiller, M. Cloitre, C. Clasen, D. Vlassopoulos, and W. Briels, "Nonmonotonic stress relaxation after cessation of steady shear flow in supramolecular assemblies," Physical review letters **123** (2019), 10.1103/PhysRevLett.123.218003.
[65]J. Mewis and N. J. Wagner, "Thixotropy," Advances in Colloid and Interface Science **147-148**, 214–227 (2009), colloids, polymers and surfactants.Special Issue in honour of Brian Vincent.
[66]R. G. Larson and Y. Wei, "A review of thixotropy and its rheological modeling," Journal of Rheology **63**, 477–501 (2019).
[67]S. Jamali, R. C. Armstrong, and G. H. McKinley, "Multiscale nature of thixotropy and rheological hysteresis in attractive colloidal suspensions under shear," Phys. Rev. Lett. **123**, 248003 (2019).
[68]D. J. Pine, J. P. Gollub, J. F. Brady, and A. M. Leshansky, "Chaos and threshold for irreversibility in sheared suspensions," Nature **438**, 997–1000 (2005).
[69]C. Carotenuto, G. Rexha, R. Martone, and M. Minale, "The microstructural change causing the failure of the cox-merz rule in newtonian suspensions: experiments and simulations," Rheologica Acta **60**, 309–325 (2021).
[70]D. P. Kalman and N. J. Wagner, "Microstructure of shear-thickening concentrated suspensions determined by flow-usans," Rheologica Acta **48**, 897–908 (2009).
[71]S. A. Shah, Y.-L. Chen, K. S. Schweizer, and C. F. Zukoski, "Viscoelasticity and rheology of depletion flocculated gels and fluids," The Journal of Chemical Physics **119**, 8747–8760 (2003).
[72]A. Sierou and J. F. Brady, "Rheology and microstructure in concentrated noncolloidal suspensions," Journal of Rheology **46**, 1031–1056 (2002).
[73]H. J. Wilson, "An analytic form for the pair distribution function and rheology of a dilute suspension of rough spheres in plane strain flow," Journal of Fluid Mechanics **534**, 97–114 (2005).
[74]J. R. Melrose and R. C. Ball, ""contact networks" in continuously shear thickening colloids," Journal of Rheology **48**, 961–978 (2004).
[75]M. G. Hansen and F. Nazem, "Transient Normal Force Transducer Response in a Modified Weissenberg Rheogoniometer," Transactions of The Society of Rheology **19**, 21–36 (1975).
[76]A. Ahuja, A. Potanin, and Y. M. Joshi, "Two step yielding in soft materials," Advances in Colloid and Interface Science **282**, 102179 (2020).
[77]E. Moghimi and G. Petekidis, "Mechanisms of two-step yielding in attractive colloidal glasses," Journal of Rheology **64**, 1209–1225 (2020).

PLEASE CITE THIS ARTICLE AS DOI: 10.1122/8.0000688

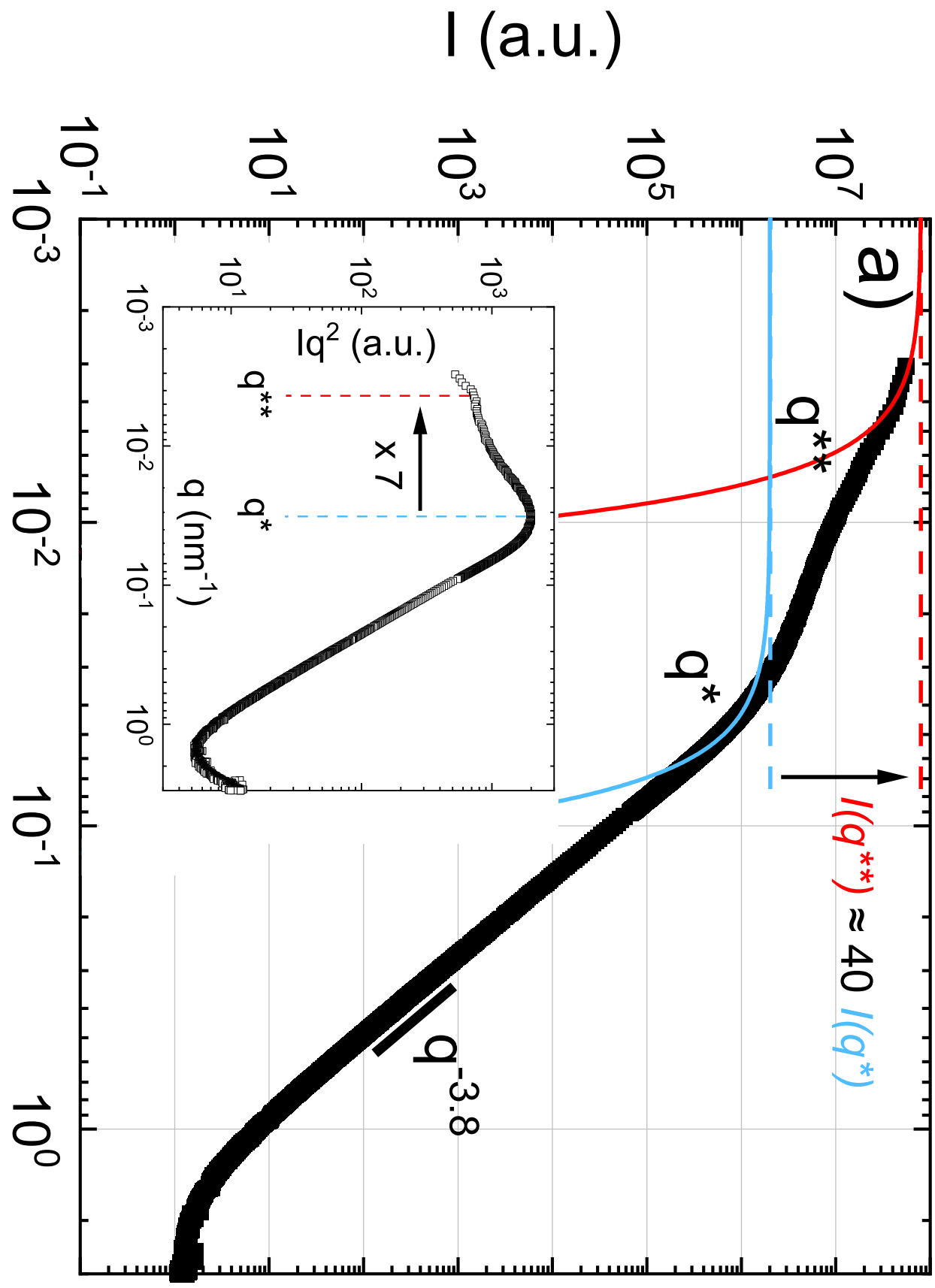

Journal of Rheology

Journal of Rheology

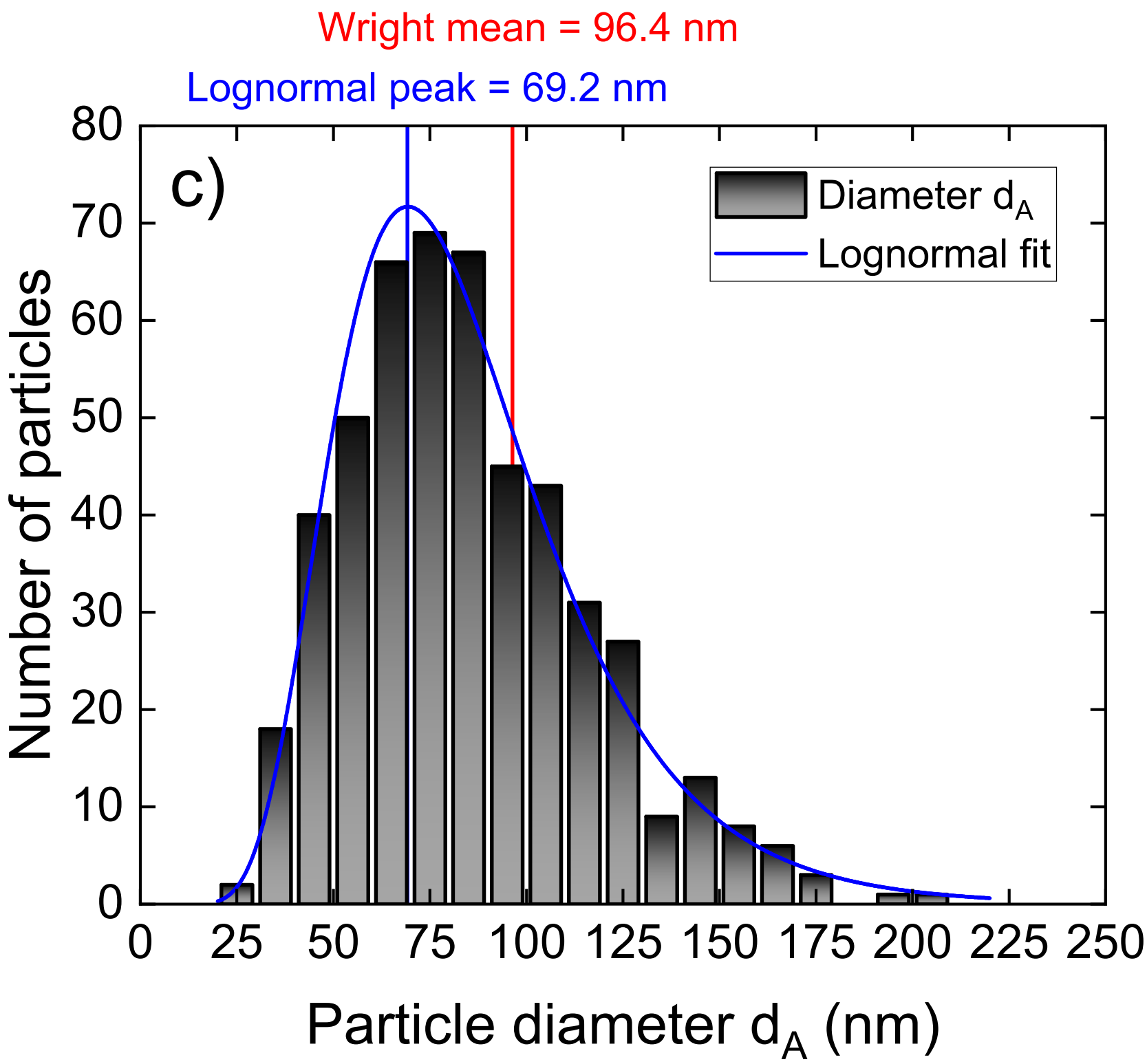

Journal of Rheology ACCEPTED MANUSCRIPT

This is the author's peer reviewed, accepted manuscript. However, the online version of record will be different from this version once it has been copyedited and typeset.
PLEASE CITE THIS ARTICLE AS DOI: 10.1122/8.0000688

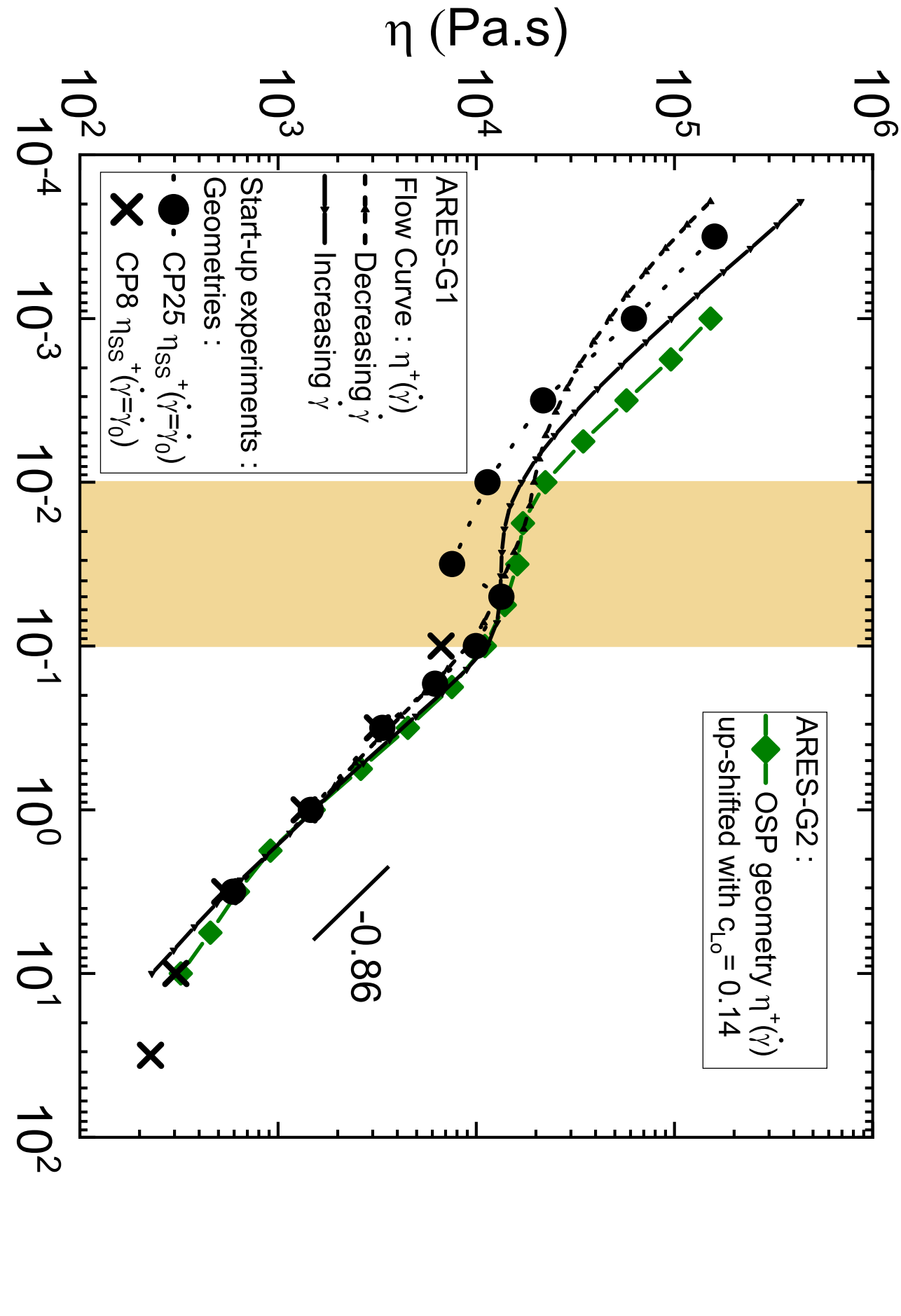

πάντα ῥεῖ

Journal of Rheology

ACCEPTED MANUSCRIPT

This is the author's peer reviewed, accepted manuscript. However, the online version of record will be different from this version once it has been copyedited and typeset.
PLEASE CITE THIS ARTICLE AS DOI: 10.1122/8.0000688

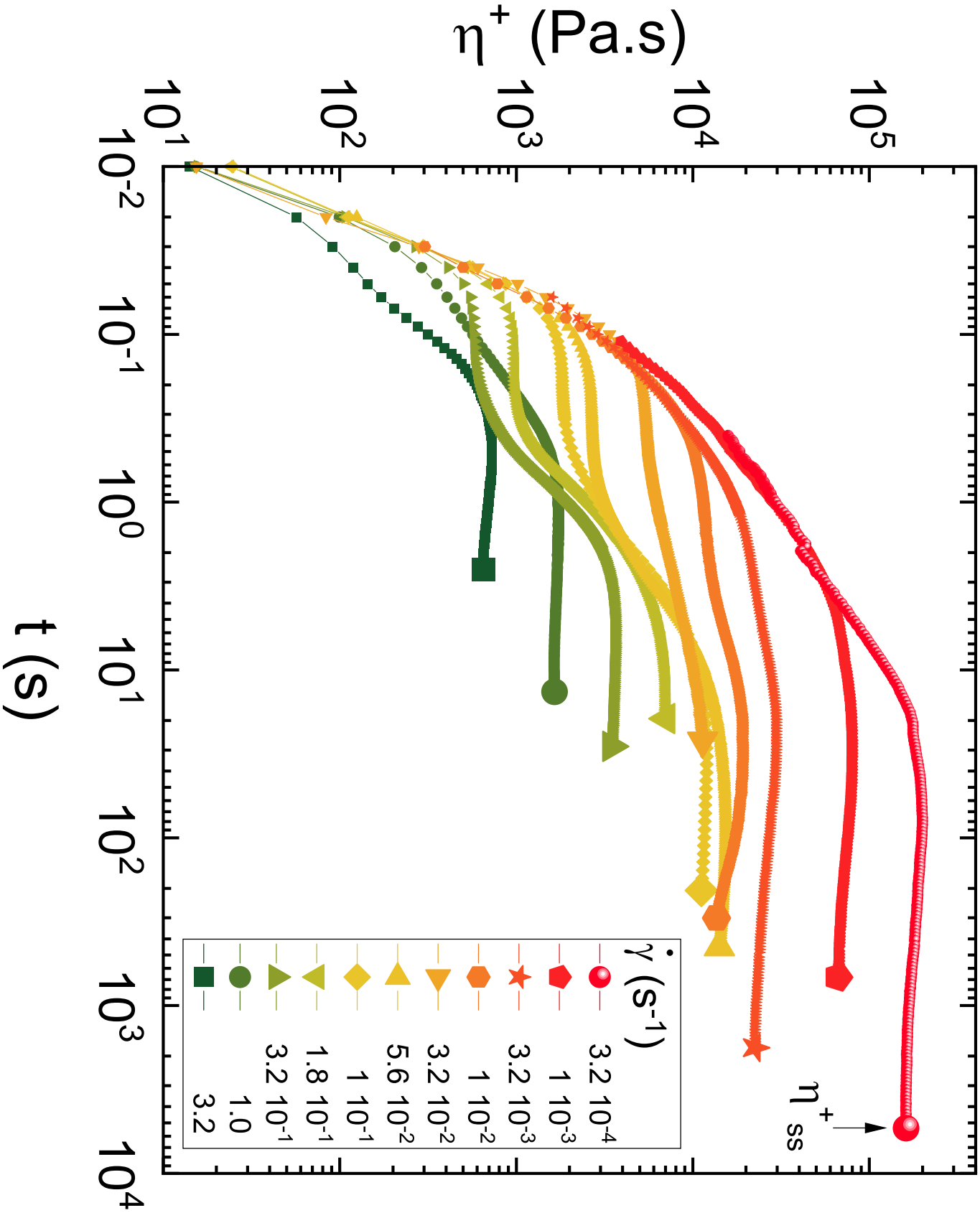

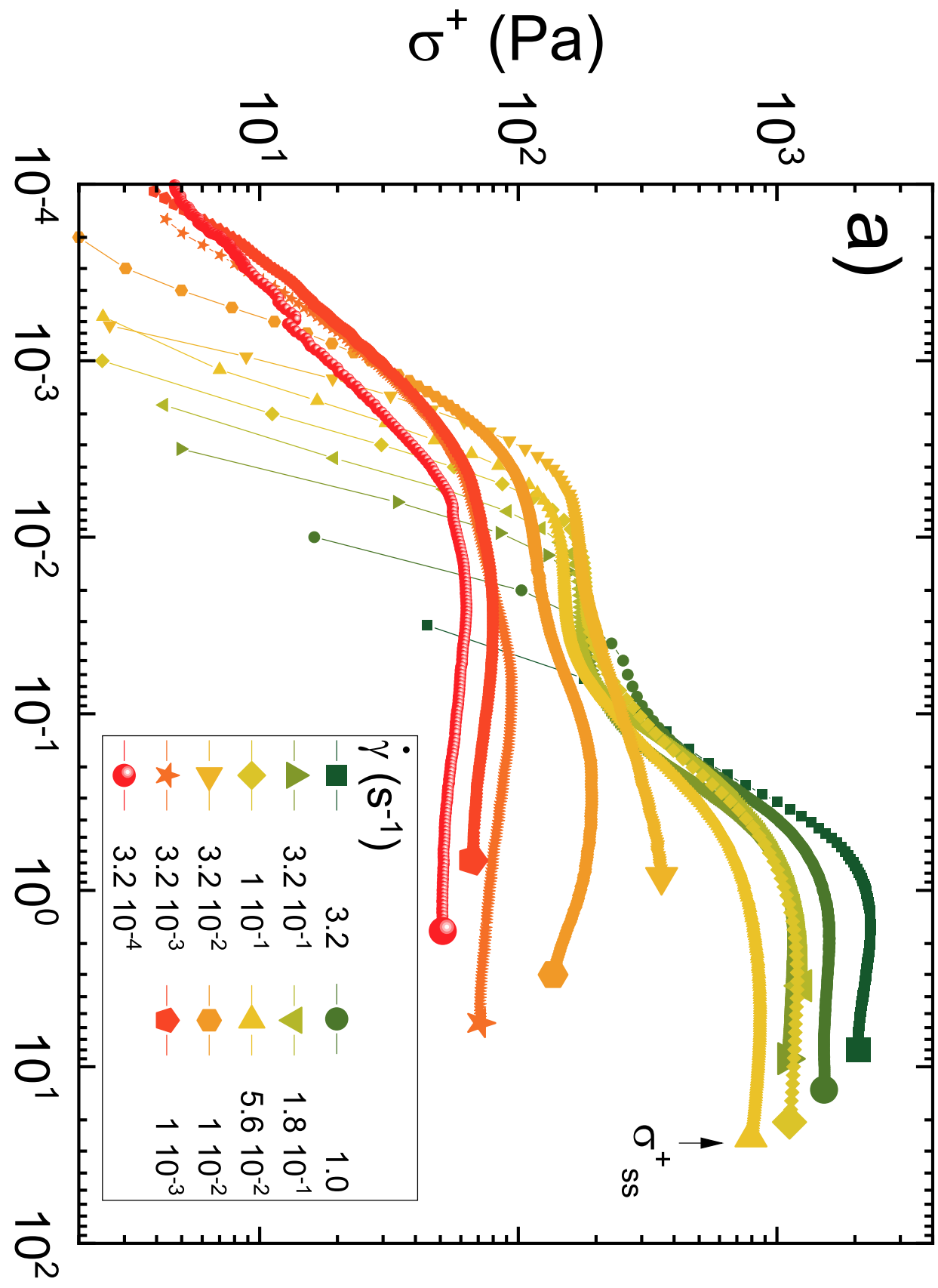

PLEASE CITE THIS ARTICLE AS DOI: 10.1122/8.0000688

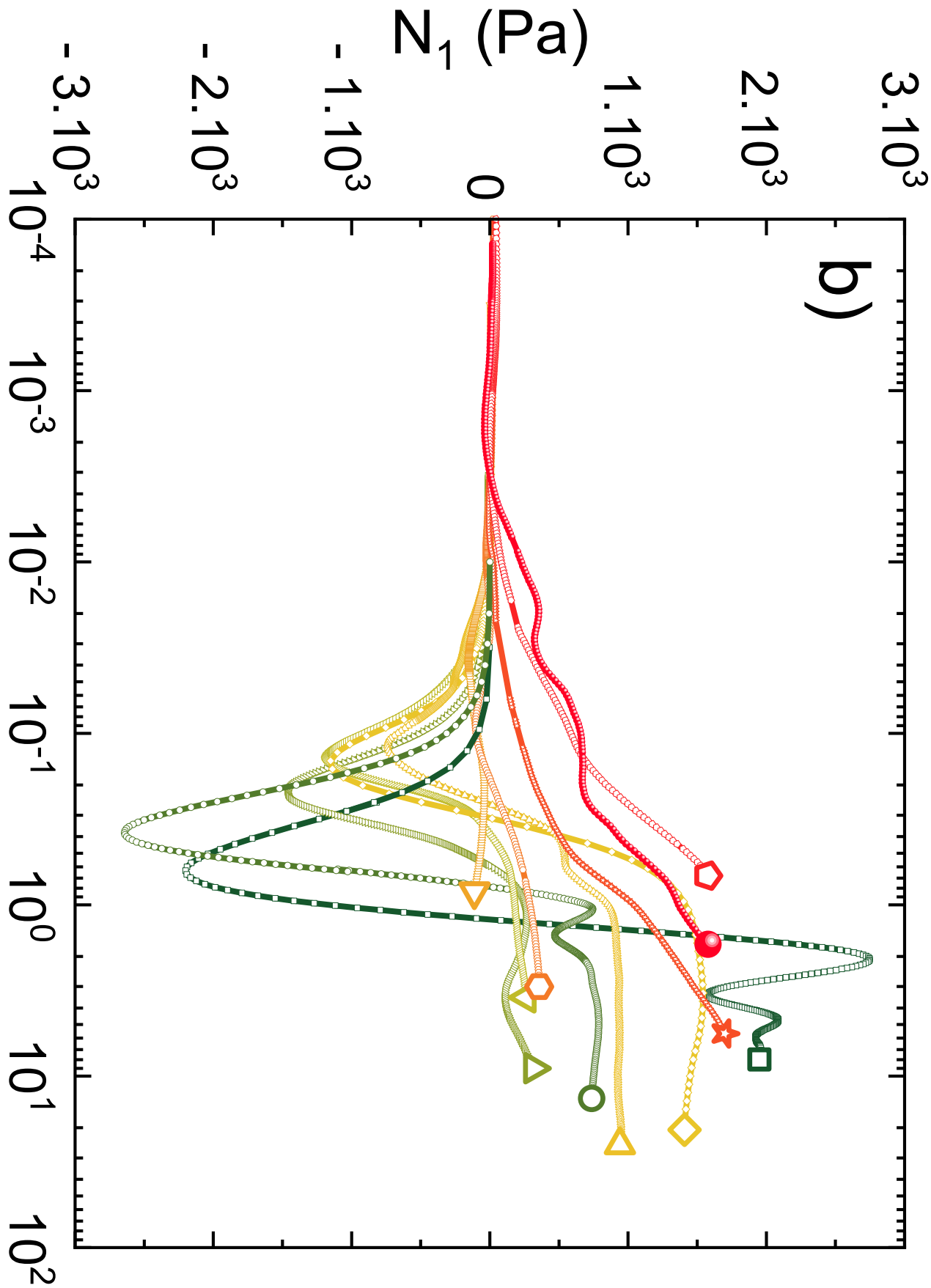

Journal of Rheology ACCEPTED MANUSCRIPT

This is the author's peer reviewed, accepted manuscript. However, the online version of record will be different from this version once it has been copyedited and typeset.
PLEASE CITE THIS ARTICLE AS DOI: 10.1122/8.0000688

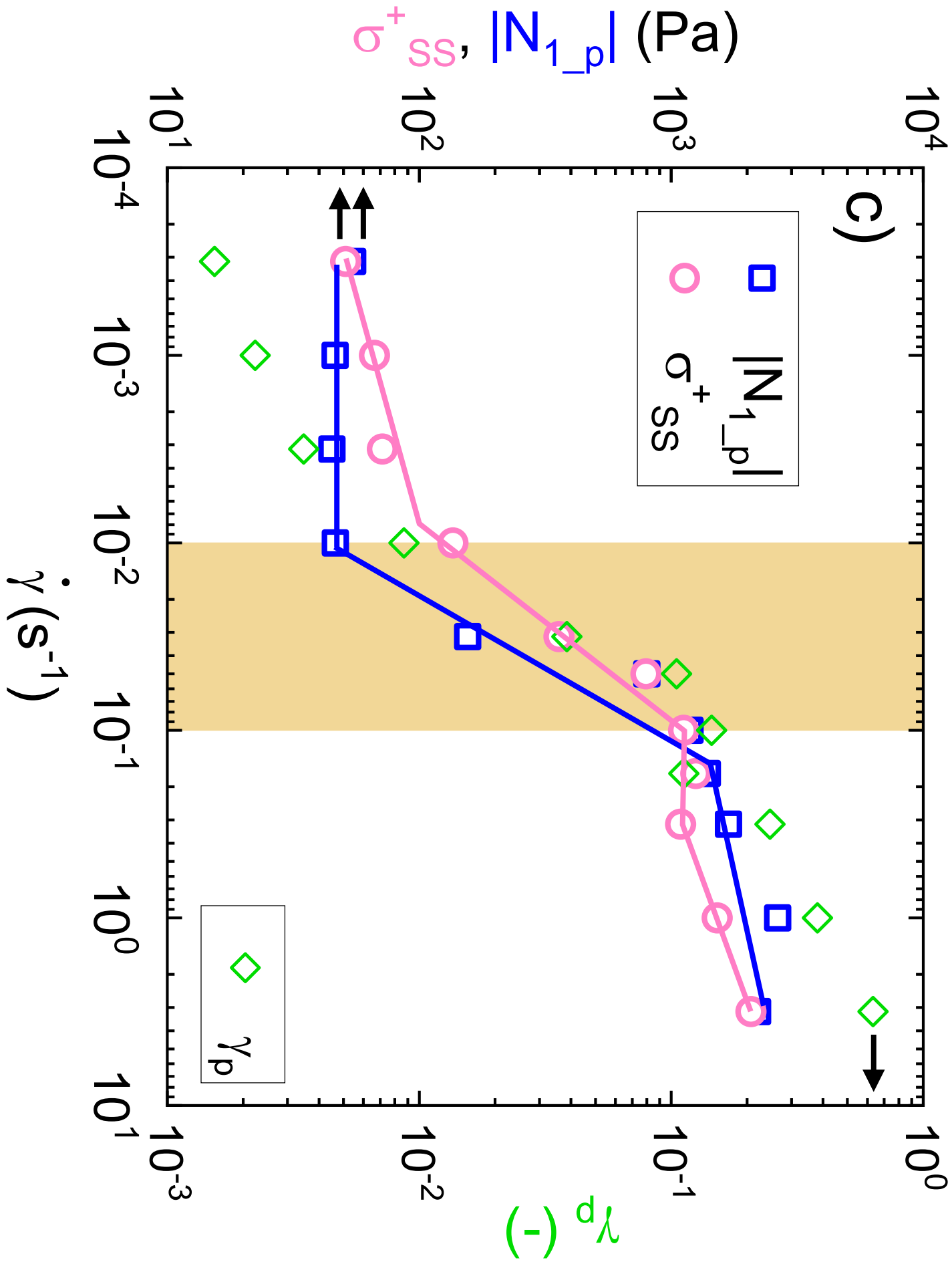

PLEASE CITE THIS ARTICLE AS DOI: 10.1122/8.0000688

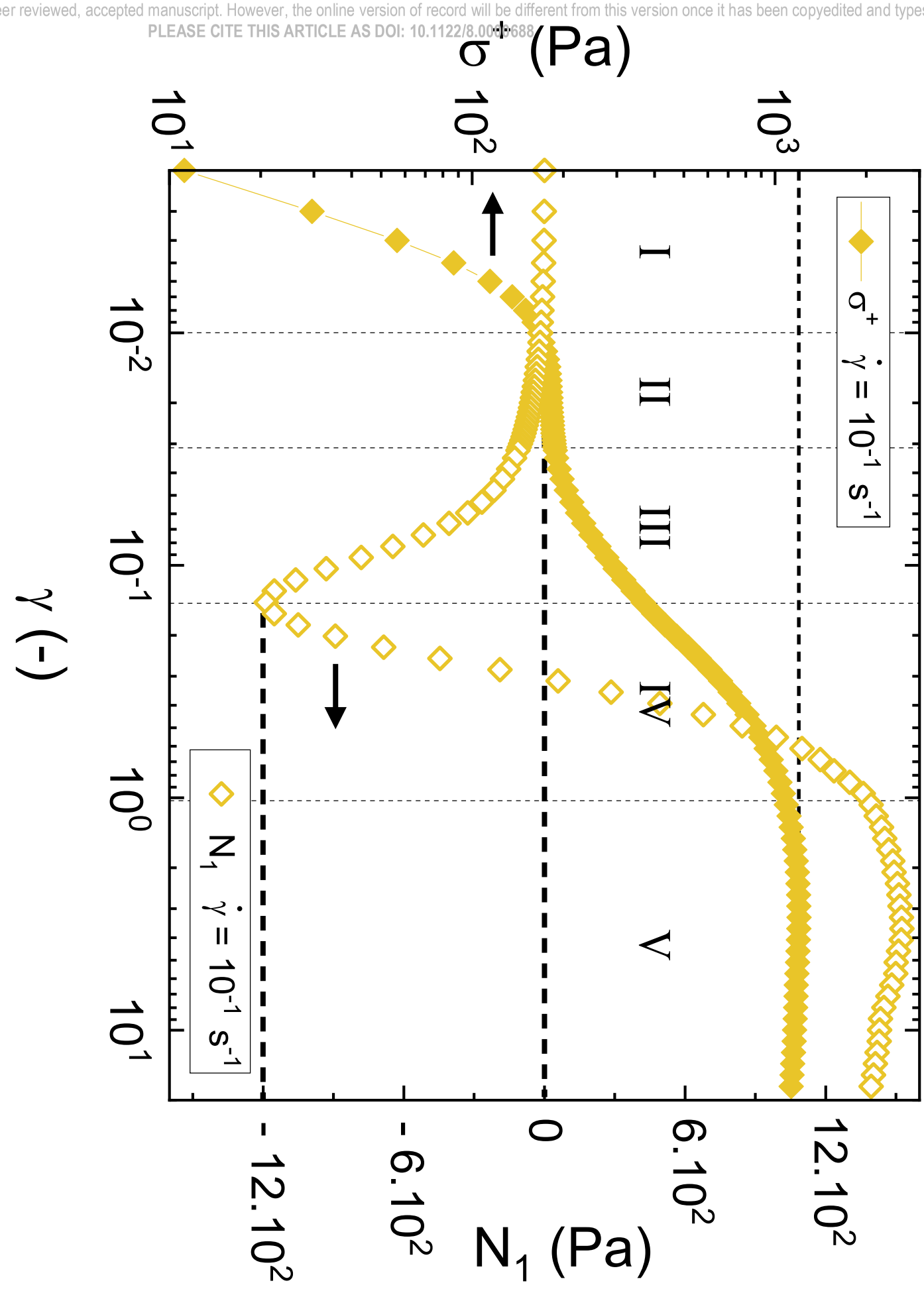

Journal of Rheology

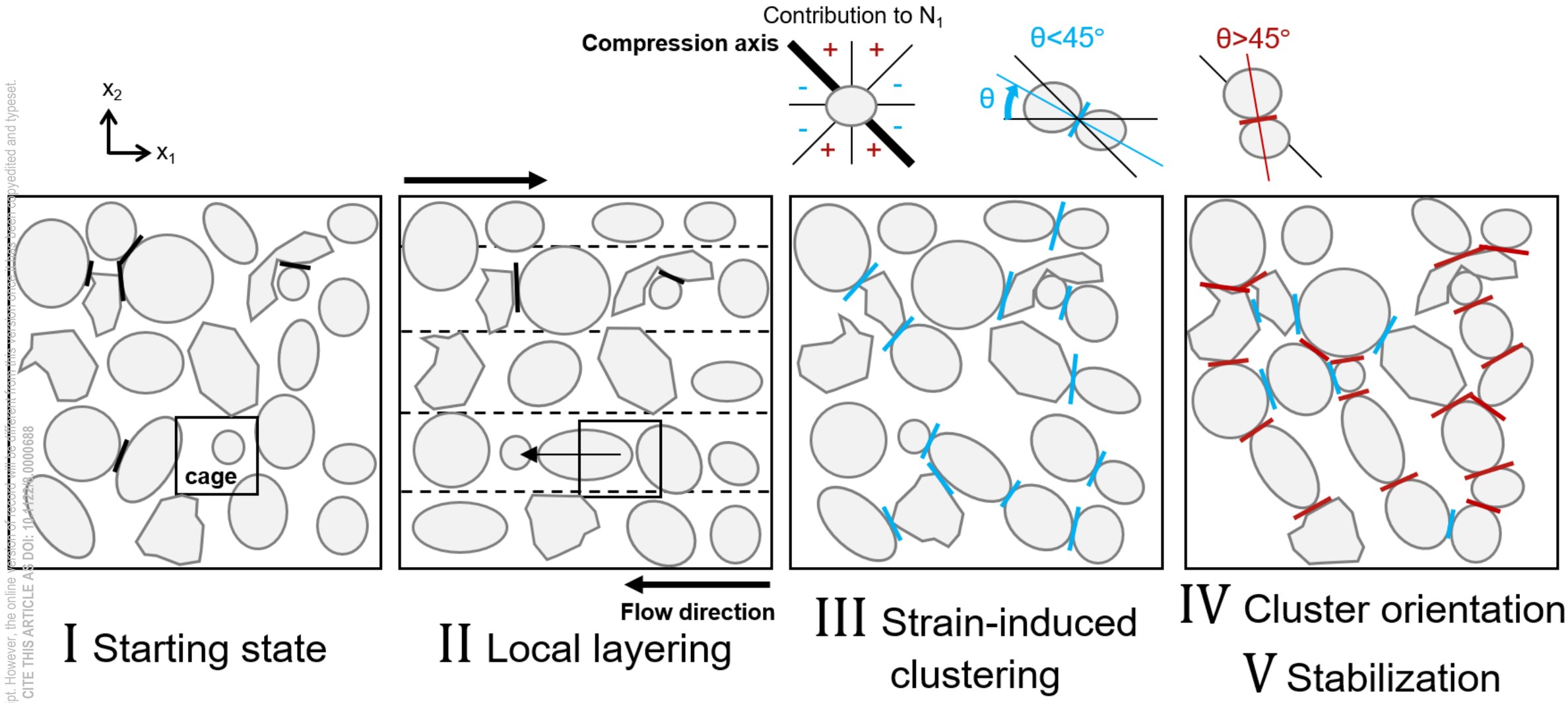

Journal of Rheology ACCEPTED MANUSCRIPT

This is the author's peer reviewed, accepted manuscript. However, the online version of record will be different from this version once it has been copyedited and typeset.
PLEASE CITE THIS ARTICLE AS DOI: 10.1122/8.0000688

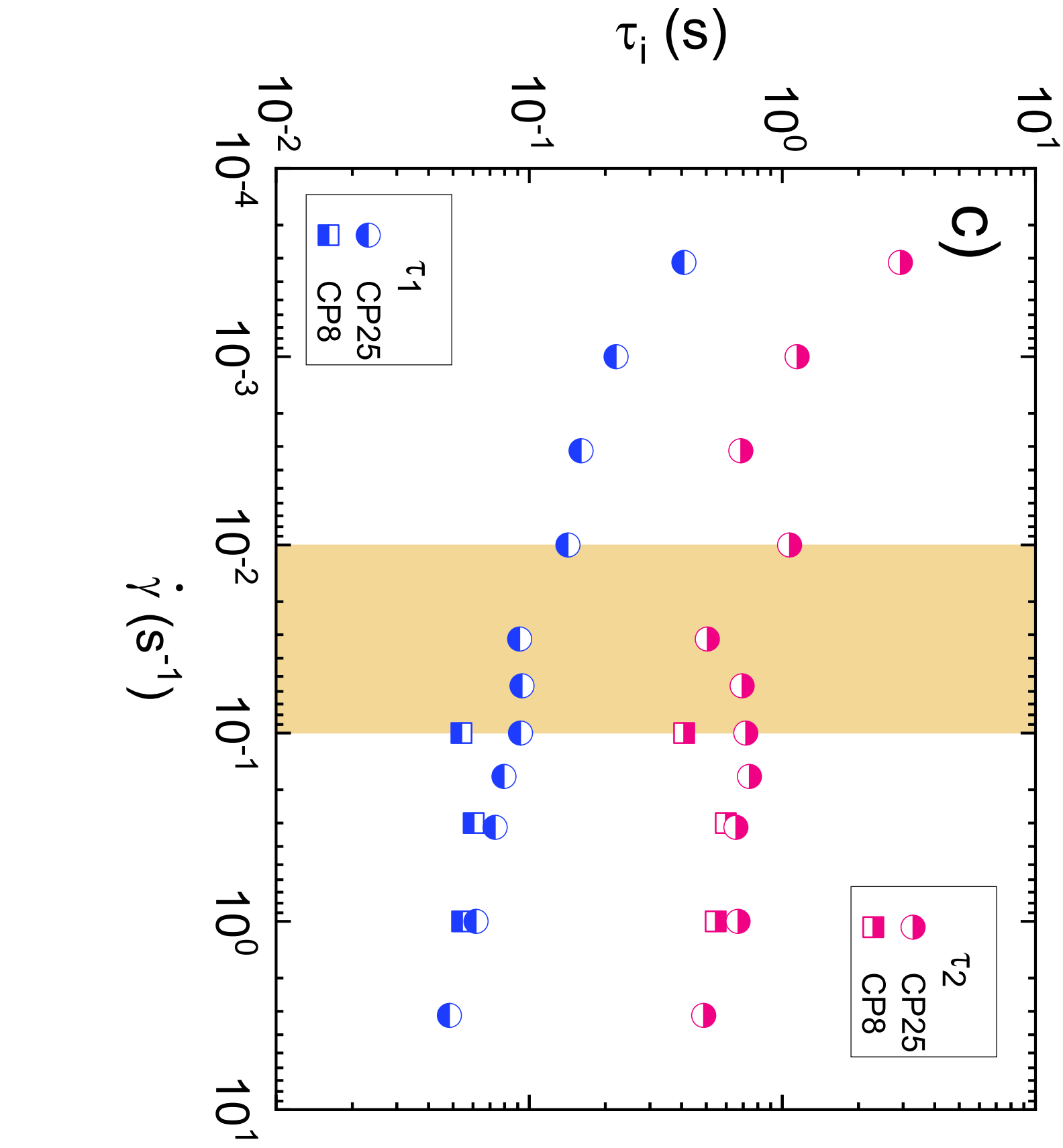

πάντα ρεῖ

Journal of Rheology

ACCEPTED MANUSCRIPT

This is the author's peer reviewed, accepted manuscript. However, the online version of record will be different from this version once it has been copyedited and typeset.
PLEASE CITE THIS ARTICLE AS DOI: 10.1122/8.0000688

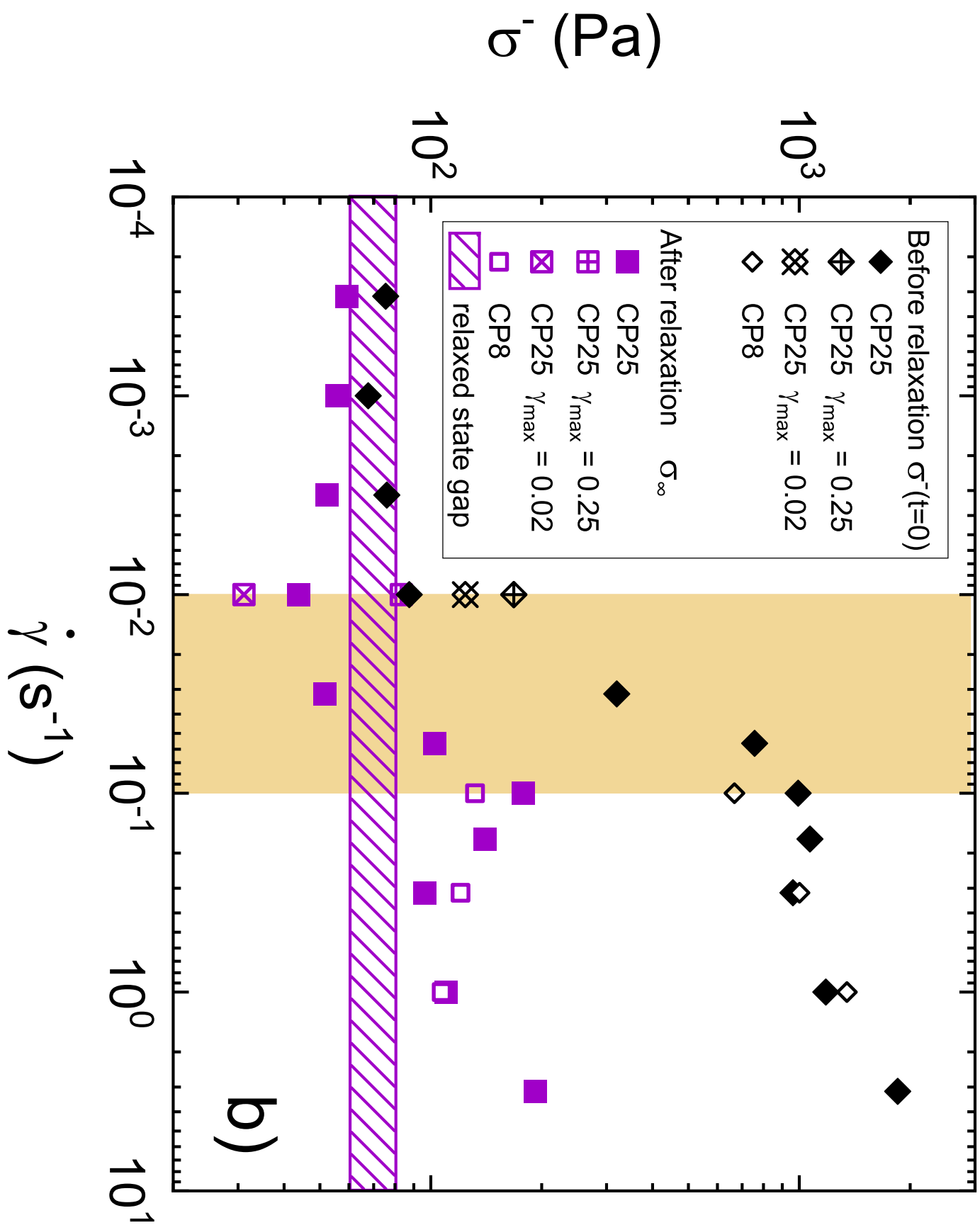

Journal of Rheology ACCEPTED MANUSCRIPT

This is the author's peer reviewed, accepted manuscript. However, the online version of record will be different from this version once it has been copyedited and typeset.
PLEASE CITE THIS ARTICLE AS DOI: 10.1122/8.0000688

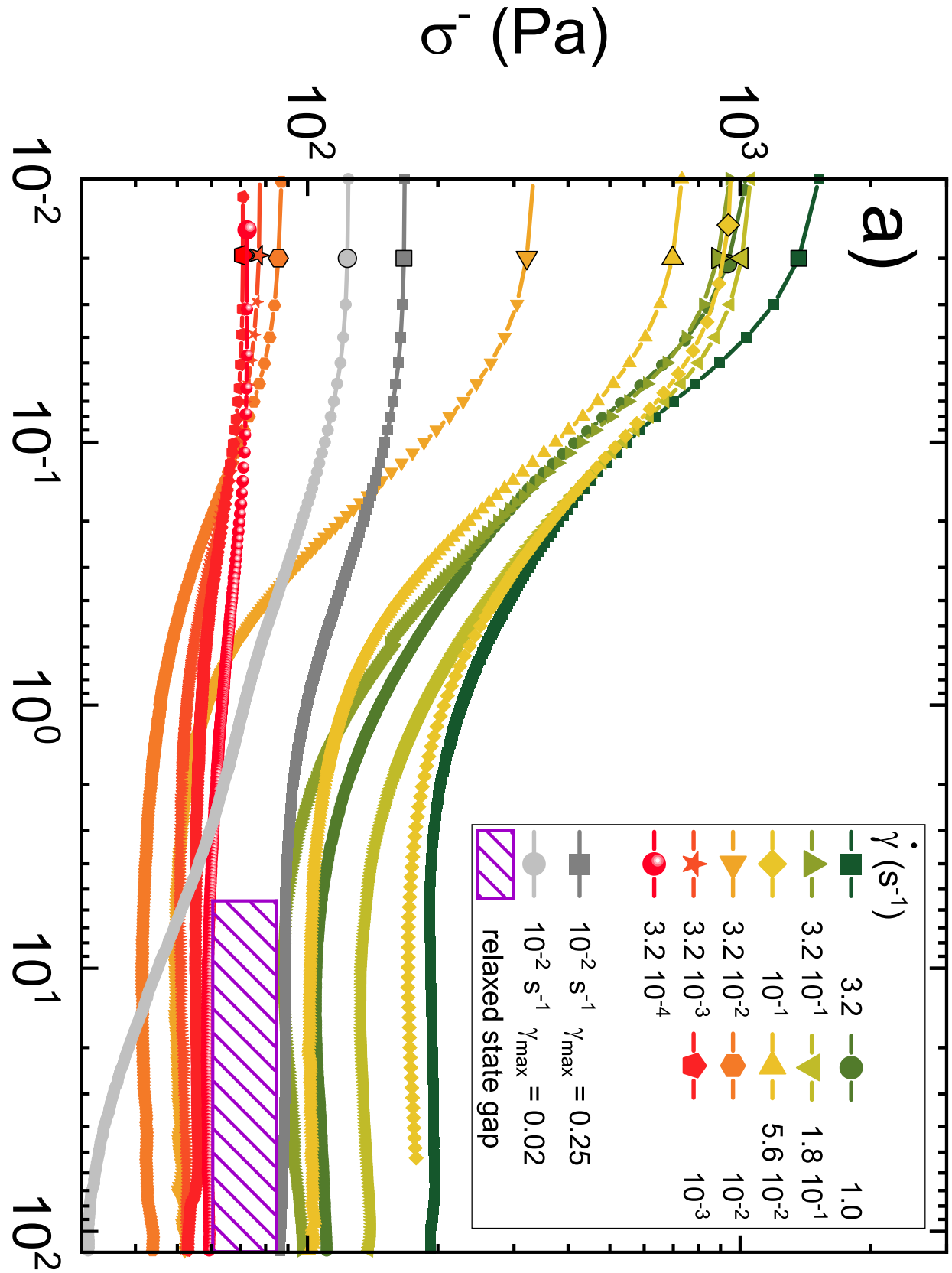

Journal of Rheology ACCEPTED MANUSCRIPT

PLEASE CITE THIS ARTICLE AS DOI: 10.1122/8.0000688

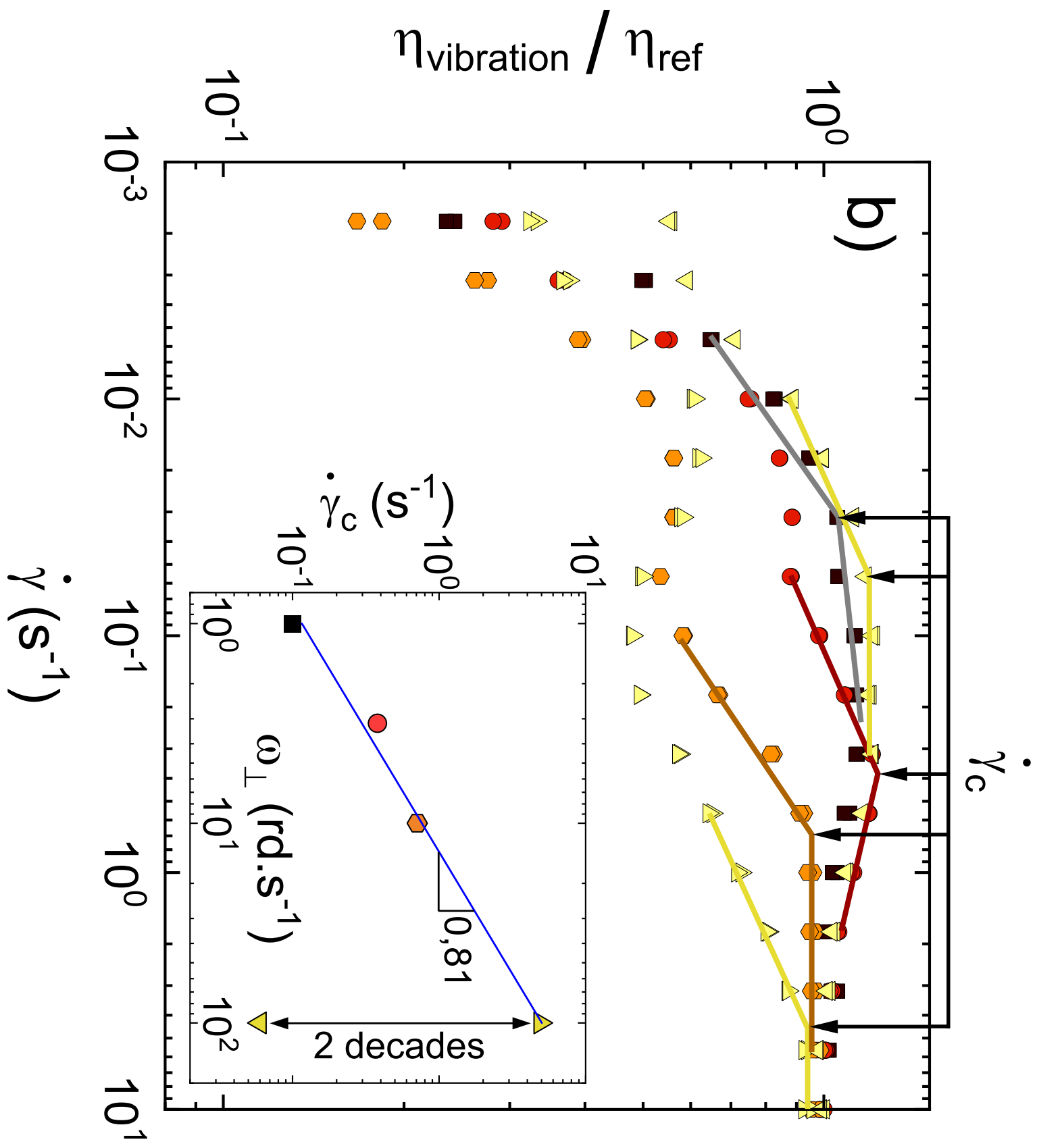

PLEASE CITE THIS ARTICLE AS DOI: 10.1122/8.0000688

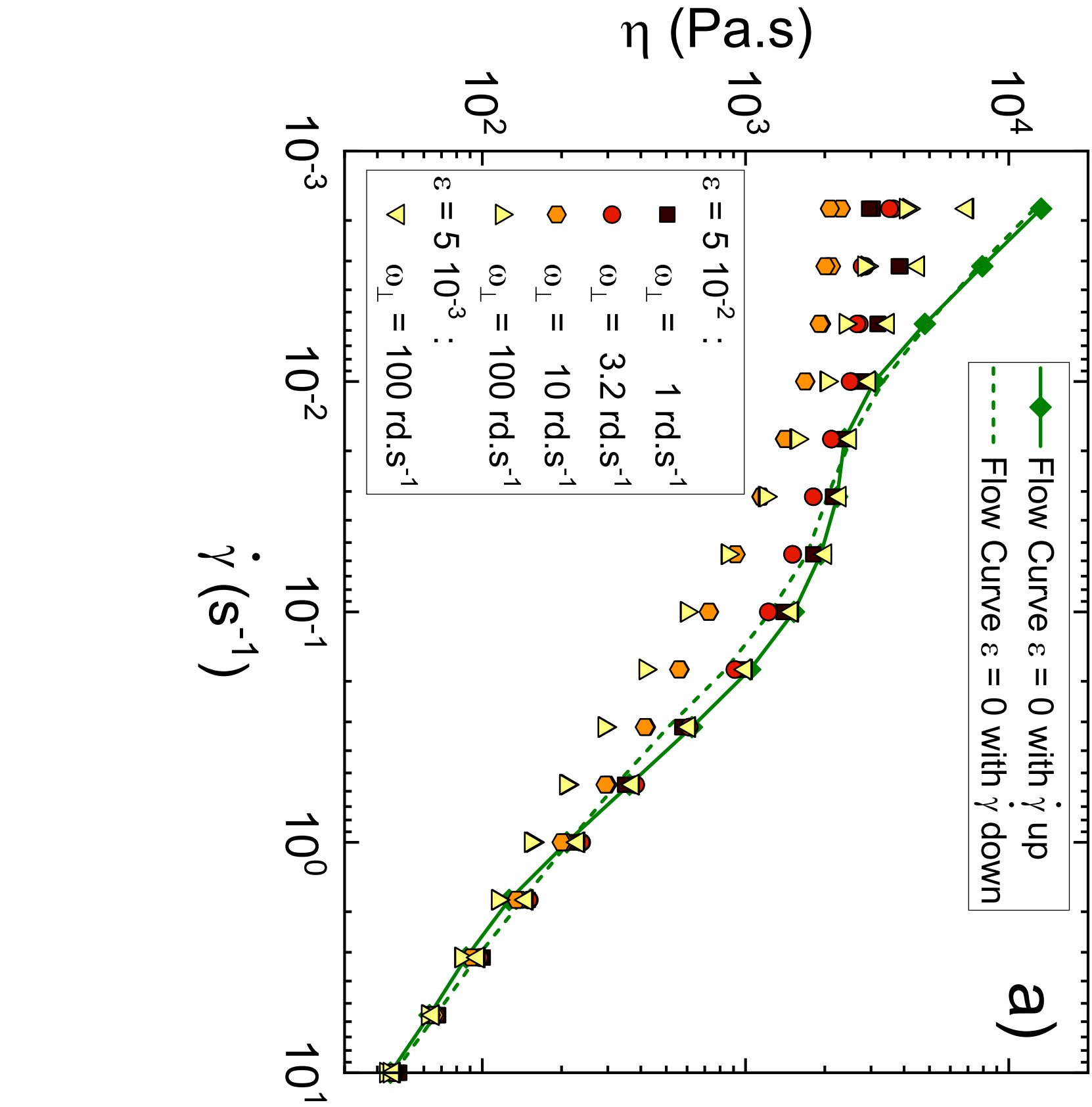

Journal of Rheology ACCEPTED MANUSCRIPT

This is the author's peer reviewed, accepted manuscript. However, the online version of record will be different from this version once it has been copyedited and typeset.
PLEASE CITE THIS ARTICLE AS DOI: 10.1122/8.0000688

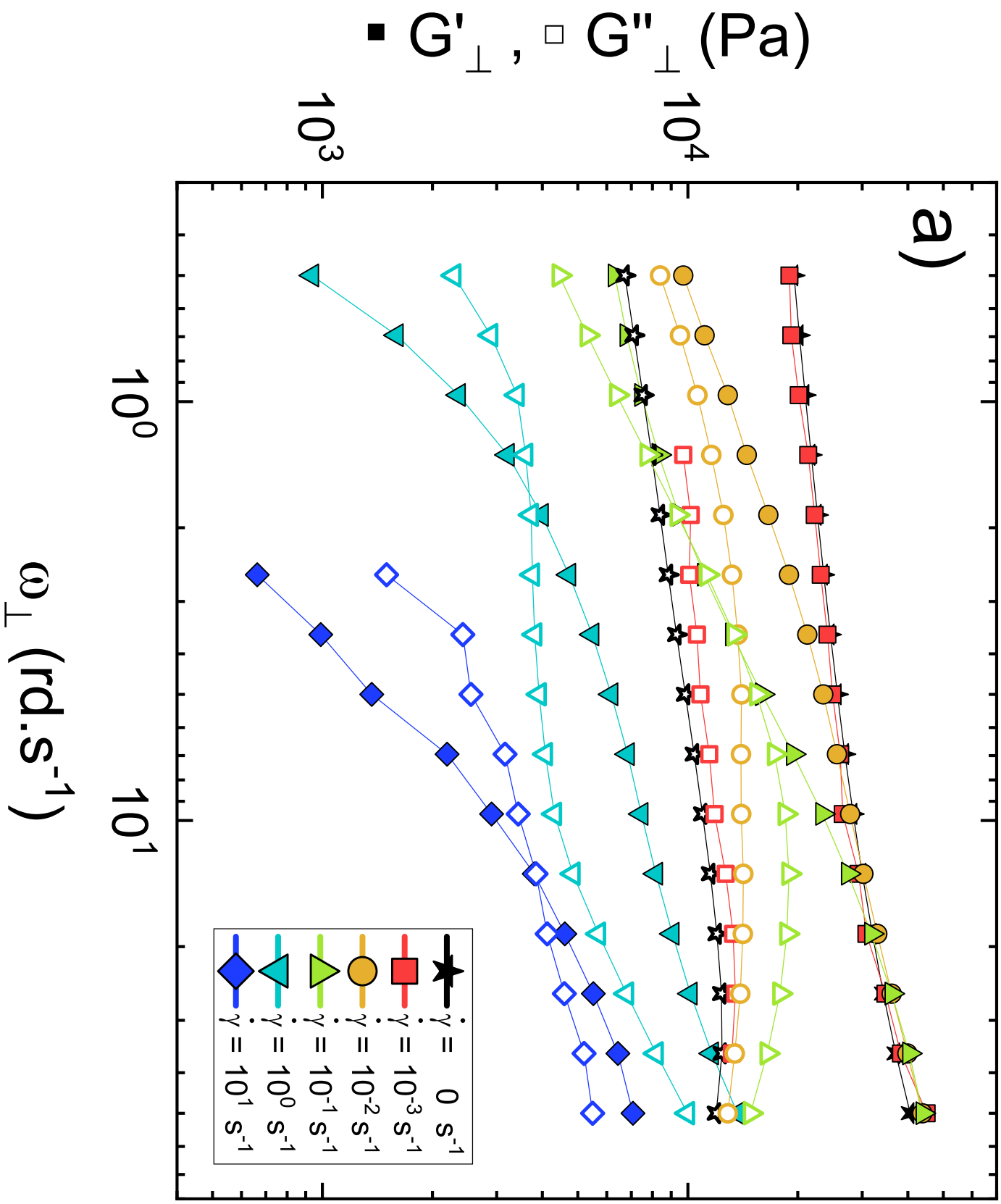

Journal of Rheology ACCEPTED MANUSCRIPT

This is the author's peer reviewed, accepted manuscript. However, the online version of record will be different from this version once it has been copyedited and typeset.
PLEASE CITE THIS ARTICLE AS DOI: 10.1122/8.0000688

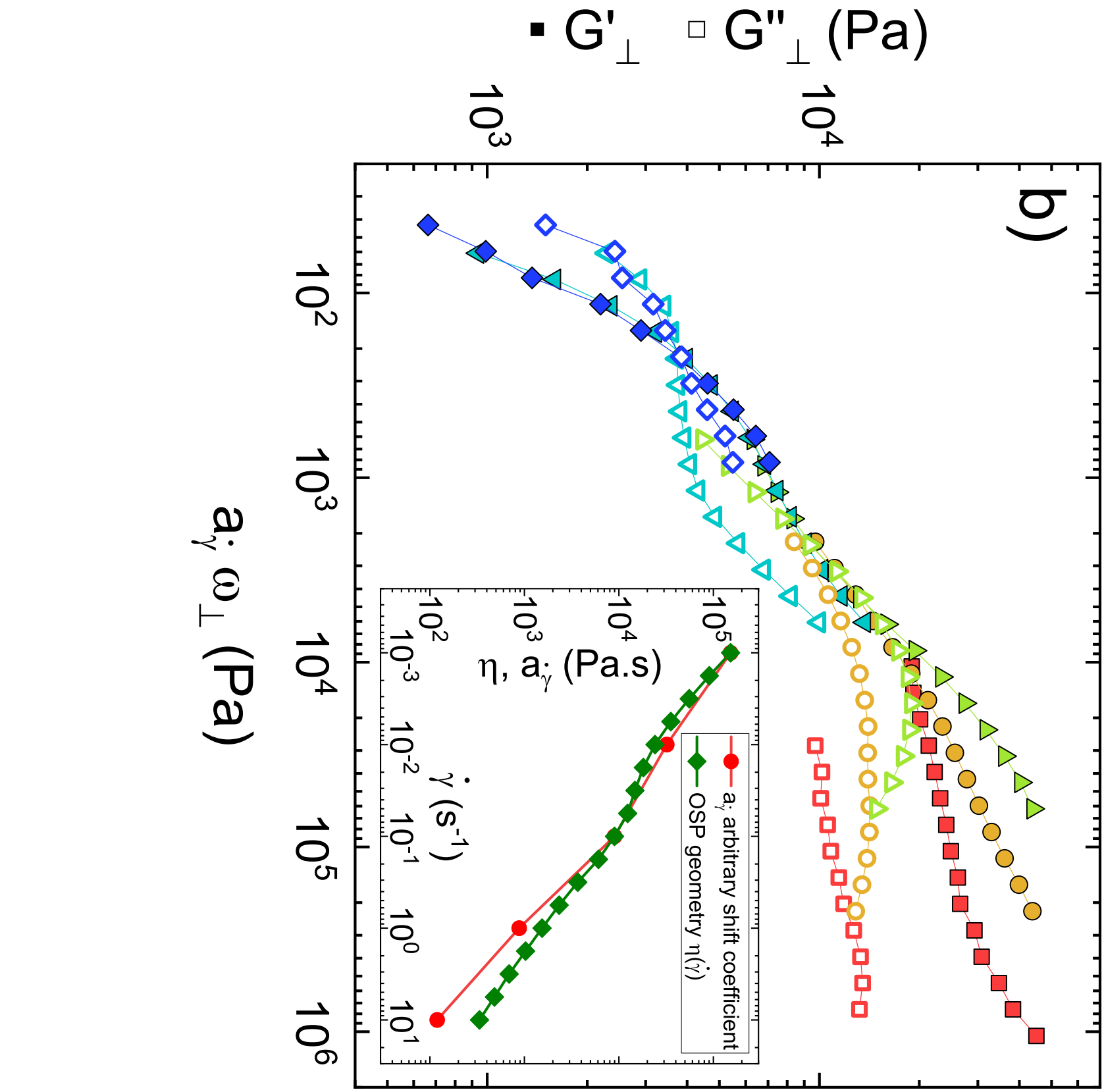

Journal of Rheology ACCEPTED MANUSCRIPT

This is the author's peer reviewed, accepted manuscript. However, the online version of record will be different from this version once it has been copyedited and typeset.
PLEASE CITE THIS ARTICLE AS DOI: 10.1122/8.0000688

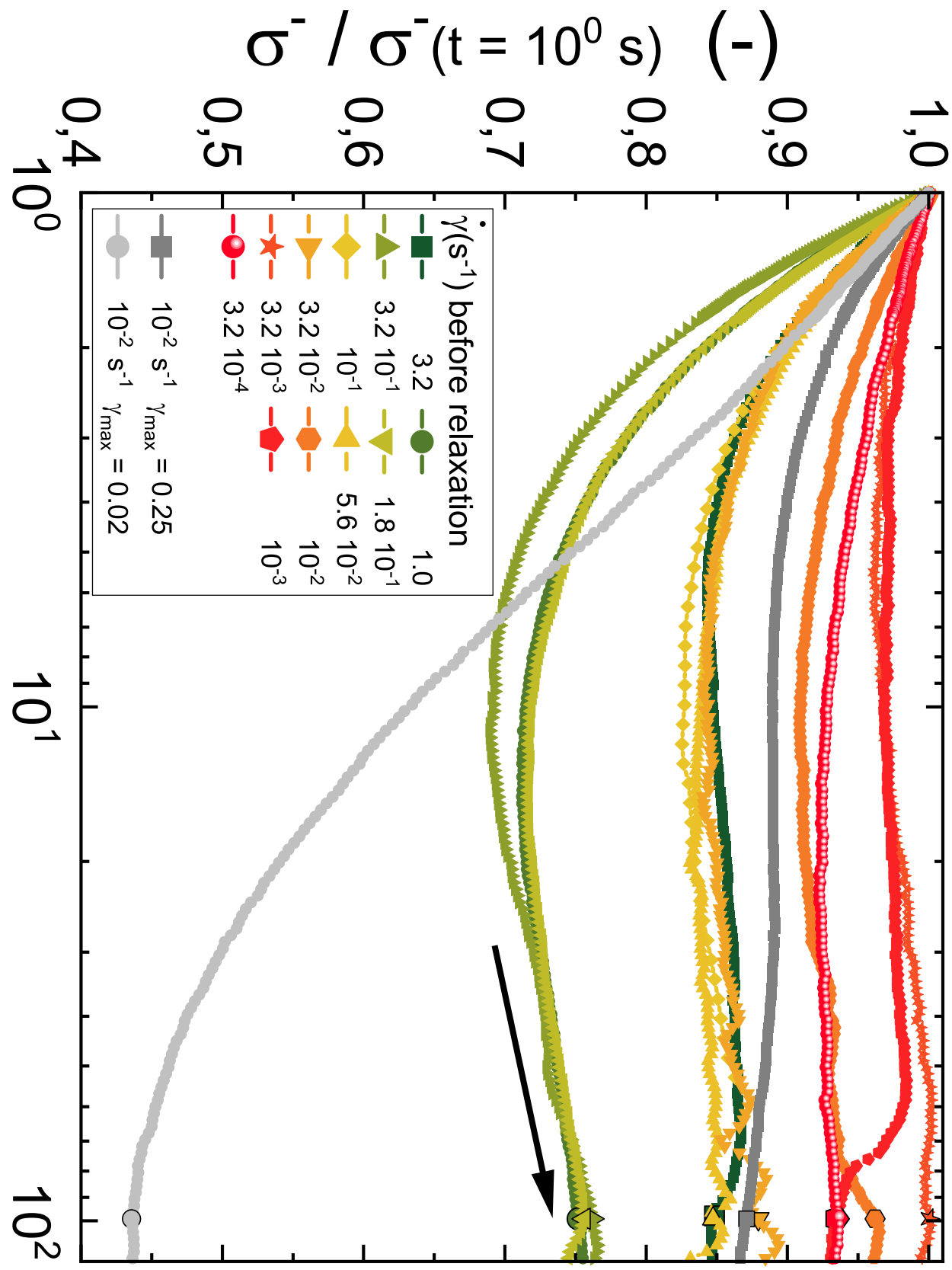

πάντα ῥεῖ
Journal of Rheology
ACCEPTED MANUSCRIPT

PLEASE CITE THIS ARTICLE AS DOI: 10.1122/8.0000688